J. Fluid Mech. (1998), *vol.* 374, *pp.* 29–57. Printed in the United Kingdom

Three-component vorticity measurements in a turbulent grid flow

By R. A. ANTONIA, T. ZHOU AND Y. ZHU†

Department of Mechanical Engineering, The University of Newcastle, N.S.W. 2308, Australia

(Received 24 November 1997 and in revised form 26 May 1998)

All components of the fluctuating vorticity vector have been measured in decaying grid turbulence using a vorticity probe of relatively simple geometry (four X-probes, i.e. a total of eight hot wires). The data indicate that local isotropy is more closely satisfied than global isotropy, the r.m.s. vorticities being more nearly equal than the r.m.s. velocities. Two checks indicate that the performance of the probe is satisfactory. Firstly, the fully measured mean energy dissipation rate $\langle\epsilon\rangle$ is in good agreement with the value inferred from the rate of decay of the mean turbulent energy $\langle q^2\rangle$ in the quasi-homogeneous region; the isotropic mean energy dissipation rate $\langle\epsilon_{iso}\rangle$ agrees closely with this value even though individual elements of $\langle\epsilon\rangle$ indicate departures from isotropy. Secondly, the measured decay rate of the mean-square vorticity $\langle\omega^2\rangle$ is consistent with that of $\langle q^2\rangle$ and in reasonable agreement with the isotropic form of the transport equation for $\langle\omega^2\rangle$. Although $\langle\epsilon\rangle \simeq \langle\epsilon_{iso}\rangle$, there are discernible differences between the statistics of ϵ and ϵ_{iso}; in particular, ϵ_{iso} is poorly correlated with either ϵ or ω^2. The behaviour of velocity increments has been examined over a narrow range of separations for which the third-order longitudinal velocity structure function is approximately linear. In this range, transverse velocity increments show larger departures than longitudinal increments from predictions of Kolmogorov (1941). The data indicate that this discrepancy is only partly associated with differences between statistics of locally averaged ϵ and ω^2, the latter remaining more intermittent than the former across this range. It is more likely caused by a departure from isotropy due to the small value of R_λ, the Taylor microscale Reynolds number, in this experiment.

1. Introduction

Measurements of one, two and in some cases all three components of the vorticity vector ω_i ($\equiv \epsilon_{ijk}u_{k,j}$, where ϵ_{ijk} is the alternating tensor and $u_{k,j} = \partial u_k/\partial x_j$; unless specifically noted, the summation convention applies) have been reported in different flows using different types of hot-wire probes (e.g. Wallace & Foss 1995; Antonia, Zhu & Shafi 1996*b*; Zhu & Antonia 1996, 1997). An accurate measurement of ω_i is important for studying various aspects of turbulence, for example the turbulent/non-turbulent interface and small-scale intermittency. In this context, it is reasonable to turn to grid turbulence when seeking to validate the performance of a new probe, especially one which measures a quantity as complex as vorticity. The existence of a region, first occurring some distance downstream from the grid (after the grid-generated wakes have merged), which can be considered to be approximately homogeneous and isotropic (see, for example, Mohamed & LaRue 1990), allows

† Current Address: Advanced Fluid Dynamics Laboratory, CSIRO Division of Building, Construction and Engineering, PO Box 56, Graham Road, Highett, Vic. 3190, Australia.

considerable simplifications to the transport equations for the mean turbulent energy $\langle u_i u_i \rangle \equiv \langle q^2 \rangle$ (angular brackets denote time averaging) and the mean-square vorticity or enstrophy $\langle \omega_i \omega_i \rangle \equiv \langle \omega^2 \rangle$. The equation describing the rate of change of $\langle q^2 \rangle$ reduces to

$$-U_1 \frac{\mathrm{d}}{\mathrm{d}x_1}\left(\frac{1}{2}\langle q^2 \rangle\right) = \langle \epsilon \rangle, \tag{1.1}$$

where U_1 is the (constant) longitudinal mean velocity.

Von Kármán (1937) first derived the equation describing the rate of change of $\langle \omega^2 \rangle$ for homogeneous isotropic turbulence

$$-U_1 \frac{\mathrm{d}\langle \omega^2 \rangle}{\mathrm{d}x_1} = 2\langle \omega_i \omega_j u_{i,j} \rangle + 2\nu \langle \omega_i \nabla^2 \omega_i \rangle, \tag{1.2}$$

where ν is the kinematic viscosity. The first term on the right corresponds to the creation of $\langle \omega^2 \rangle$ through the deformation of vortex tubes and the second term, which represents the destruction of $\langle \omega^2 \rangle$ through the action of viscosity, is related to the mean palinstrophy or mean-squared value of the curl of the vorticity vector (e.g. Frisch 1995; Lesieur 1997). Von Kármán & Howarth (1938) pointed out that (1.2) is equivalent to the limiting form of the equation describing the transport of the two-point longitudinal velocity correlation function f in homogeneous isotropic turbulence when the separation between the two points approaches zero. Taylor (1938) quantified the importance of the vortex stretching term through measurements of $\langle u_1^2 \rangle$ and f. Batchelor & Townsend (1947, hereafter BT), used hot-wire measurements of u_1 and of its first two temporal derivatives ($\partial u_1/\partial t$ and $\partial^2 u_1/\partial t^2$) downstream of a grid to estimate the isotropic forms of all the terms in (1.2). Specifically, they considered

$$-U_1 \frac{\mathrm{d}\langle \omega^2 \rangle}{\mathrm{d}x_1} = -\frac{7}{\sqrt{5}}\langle \omega^2 \rangle^{3/2} S - \frac{14}{\sqrt{5}}\langle \omega^2 \rangle^{3/2} \frac{G}{R_\lambda} \tag{1.3}$$

with $\langle \omega^2 \rangle$ replaced by its isotropic value, i.e. $15\langle u_{1,1}^2 \rangle$. In (1.3), S is the skewness of $u_{1,1}$ (like Taylor 1938, BT emphasized the relationship between the vorticity production term and the probability distribution of the rate of extension of fluid line elements aligned in any given direction), G is the ratio $\langle u_1^2 \rangle \langle u_{1,11}^2 \rangle / \langle u_{1,1}^2 \rangle^2$ (note that $u_{1,11} \equiv \partial^2 u_1/\partial x_1^2$) and R_λ is the Taylor microscale Reynolds number ($R_\lambda = \langle u_1^2 \rangle^{1/2} \lambda / \nu$, with the Taylor microscale $\lambda \equiv \langle u_1^2 \rangle^{1/2} / \langle u_{1,1}^2 \rangle^{1/2}$). The measurements of BT indicated that both S and G/R_λ were approximately constant throughout the decay so that $\langle \omega^2 \rangle^{1/2}$ varied inversely proportional to x_1 (the distance from the grid), namely

$$\langle \omega^2 \rangle^{1/2} \sim x_1^{-1}. \tag{1.4}$$

It should be noted that this '−1' decay rate is consistent with the '−1' decay rate exhibited by $\langle u_1^2 \rangle$ in BT's experiment. In general, $\langle q^2 \rangle \sim x_1^{-n}$ with n typically in the range 1 to 1.3 (e.g. Batchelor & Townsend 1948; Comte-Bellot & Corrsin 1966), so that $\langle \epsilon \rangle \sim x^{-1-n}$ and, if the turbulence is homogeneous ($\langle \epsilon \rangle = \nu \langle \omega^2 \rangle$), $\langle \omega^2 \rangle \sim x^{-1-n}$ (e.g. Lesieur 1997). BT concluded that their measurements satisfied (1.3) with sufficient accuracy. This conclusion appears reasonable since all the quantities in (1.3), with $\langle \omega^2 \rangle$ replaced by $\langle u_{1,1}^2 \rangle$, are primarily associated with the high-wavenumber part of the u_1 spectrum and are therefore more likely to satisfy isotropy than the individual components of $\langle u_i u_j \rangle$.

The direct measurement of vorticity should provide a more valid corroboration of (1.3) since vorticity is closely associated with the small-scale structure of turbulence

(e.g. Corrsin & Kistler 1954). Kistler (1952) tested the Kovasznay-type vorticity (ω_1) probe in grid turbulence; he noted that the high-wavenumber end of the spectrum satisfied isotropy (see figure 2 of Wallace 1986). Kit *et al.* (1988) and Fan (1991) examined the decay of $\langle\omega_1^2\rangle$ in grid turbulence as a test of their probes. Although an x_1^{-1} decay rate was found in both cases, in apparent agreement with relation (1.4), this result is strictly inconsistent with the nonlinear decay rate of $\langle u_1^2\rangle$ (i.e. $\langle u_1^2\rangle \sim x_1^{-n}$ where $n = 1.27$ for the data of Fan; Kit *et al.* did not report the decay of $\langle u_1^2\rangle$). One would therefore have to question the accuracy of the $\langle\omega_1^2\rangle$ data obtained by these authors.

The first objective of the present work was to validate the performance of a three-component vorticity probe (described in §2) by comparison with (1.1) and (1.3). The probe, with eight hot wires, is relatively simpler than the twelve-hot-wire probe used by Tsinober, Kit & Dracos (1992, hereafter TKD), or the twenty-hot-wire probe of Lemonis (1995). Both TKD and Lemonis made measurements in grid turbulence; the quality of the present data can therefore be assessed against these measurements.

TKD gave several reasons in support of the idea that grid turbulence is one of the most suitable flows for studying the universal properties of turbulence, especially its small-scale structure. Indeed, quite a number of direct numerical simulations have been carried out for either forced or decaying isotropic turbulence (e.g. Kerr 1985; Yamamoto & Hosokawa 1988; She, Jackson & Orszag 1990; Vincent & Meneguzzi 1991; Jimenez *et al.* 1993; Chen, Sreenivasan & Nelkin 1997*a*; Chen *et al.* 1997*b*; Boratav & Pelz 1997) with a view to study the kinematics and dynamics of the small-scale structure. Correspondingly, the second objective of the present work is to compare statistics of ϵ and ω^2, the instantaneous energy dissipation rate and enstrophy respectively. An attempt is made to relate the dependence on r of ϵ_r and ω_r^2 (the subscript r denotes linear averaging over a distance r) to that of the velocity increments δu_1 $[\equiv u_1(x_1 + r) - u_1(x_1)]$ and δu_2 $[\equiv u_2(x_1 + r) - u_2(x_1)]$ when the separation r is in the inertial range. δu_1 and δu_2 are identified here as the longitudinal and transverse increments. The observation that transverse velocity increments scale differently from longitudinal velocity increments is currently receiving a great deal of attention (e.g. Herweijer & van de Water 1995; Noullez *et al.* 1997; Boratav & Pelz 1997; Boratav 1997; Chen *et al.* 1997*b*; Antonia & Pearson 1997; Pearson & Antonia 1997; Camussi & Benzi 1997; Dhruva, Tsuji & Sreenivasan 1997; Grossman, Lohse & Reeh 1997). The difference in scaling, if suitably corroborated, may imply different roles played by ϵ and ω^2 (e.g. Boratav & Pelz 1997; Chen *et al.* 1997*b*) and would need to be taken into account in small-scale turbulence models. However, there is a need to reconcile the results obtained from simulations (e.g. Boratav & Pelz 1997; Chen *et al.* 1997*b*) with those inferred from measurements in grid turbulence (Kahalerras, Malecot & Gagne 1996; Camussi *et al.* 1996; Kahalerras 1997), the latter indicating approximate equality of power-law exponents for longitudinal and transverse velocity increments. This discrepancy is addressed in some detail in §7 where we consider the scaling of these increments in conjunction with the behaviour of locally averaged statistics of ϵ and ω^2.

2. Experimental details

Measurements were made along the centreline of the wind tunnel at several locations downstream of a biplane grid ($x_1/M = 20 \sim 80$, where x_1 is measured from the grid plane and the mesh size M is 24.76 mm). The grid consists of rods of 4.76 mm diameter, yielding a solidity of about 0.35. The longitudinal mean velocity

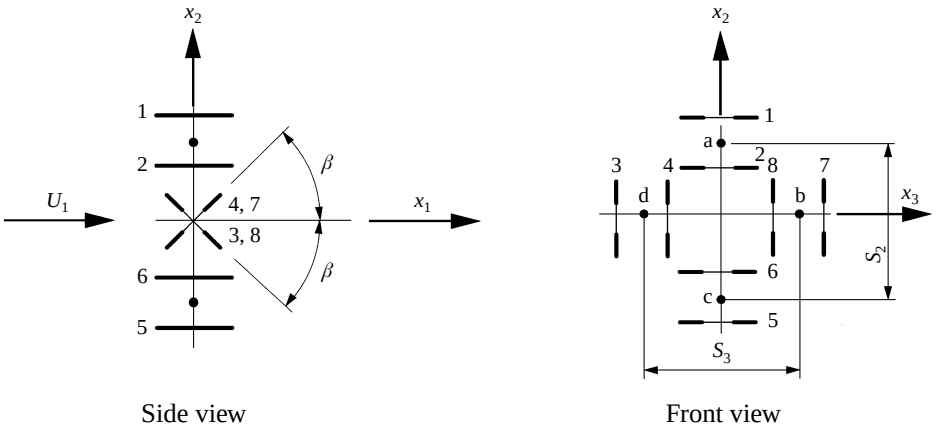

FIGURE 1. Three-component vorticity probe. $d_2 \simeq d_3 \simeq 0.6$ mm; $S_1 \simeq 0.6$ to 1.2 mm; $S_2 = 2.1$ mm; $S_3 = 2.2$ mm; $\beta \simeq 45°$; all wires have a diameter of 2.5 μm and length of 0.5 mm. (The velocity fluctuations measured by each X-probe are assumed to be at the centre of the probe.)

U_1 was 12.3 m s^{-1} (constant throughout the working section within $\pm 3\%$) and the Reynolds number R_M ($\equiv U_1 M/\nu$) was 20 300. At this speed, the Kolmogorov length scale $\eta \equiv \nu^{3/4}/\langle\epsilon\rangle^{1/4}$ varies from 0.17 mm at $x_1/M = 20$ to 0.4 mm at $x_1/M = 80$. Although the isotropic value of $\langle\epsilon\rangle$ was used for estimating η, $\langle\epsilon\rangle_{iso} \simeq \langle\epsilon\rangle$ (see §5) and this estimate is therefore reliable.

The vorticity probe consists of four X-probes (figure 1), two in the (x_1, x_2)-plane and separated in the x_3-direction; the other two in the (x_1, x_3)-plane and separated in the x_2-direction (see also Zhu & Antonia 1996, 1997). The separation between two inclined wires in each X-probe is $d_i \simeq 0.6$ mm ($i = 2, 3$). The separations between centres of X-probes are $S_2 = 2.1$ and $S_3 = 2.2$ mm in the x_2- and x_3-directions, respectively. The effective angle for each inclined wire was about 45°. For the present flow conditions, the ratio of the largest wire separation (2.2 mm) of the probe to the Kolmogorov length scale varies between about 13 ($x_1/M = 20$) and 5.7 ($x_1/M = 80$). Because of the intrinsically poor spatial resolution of the four-X-wire probe, measurements were also made for ω_2 and ω_3 respectively with a finer resolution four-wire probe. The four-wire probe, described in more detail in Antonia *et al.* (1996*b*), consists of a single X-wire whose centre is straddled by parallel hot wires (see sketch in figure 2); the probe is similar in design to that used by Foss & Haw (1990). The largest separation for this probe is 0.9 mm (the distance between the parallel hot wires). The ratio of this separation to η varies between 5.3 ($x_1/M = 20$) and 2.3 ($x_1/M = 80$). The effective angles for the X-wire are about 45°. The probe measures ω_3 when the X-wire plane coincides with the (x_1, x_2)-plane; after a 90° rotation, it measures ω_2. To study the scaling behaviour of the longitudinal and transverse velocity increments, a single X-wire probe was also used at $x_1/M = 70$ to measure u_1 and u_2. The separation of the two wires of the X-wire probe was 0.72 mm. The effective angles were about 40°. All the wires were etched from Wollaston (Pt-10% Rh) of a diameter of 2.5 μm with an active length of about 0.5 mm; the length to diameter ratio is about 200, sufficient to minimize end conduction losses.

The hot wires were operated with in-house constant temperature circuits at an overheat ratio of 0.5. Output signals from the anemometers were passed through buck and gain circuits and low-pass filtered at a cut-off frequency f_c of 5 kHz $\sim$ 10 kHz. f_c was chosen after examining the spectrum of $\partial u_1/\partial t$ and identifying the onset

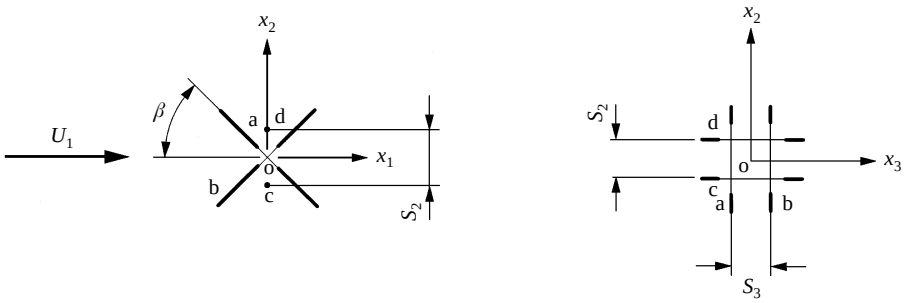

FIGURE 2. One-component vorticity probe. $S_2 = 0.9$ mm; $S_3 = 0.85$ mm; $\beta \simeq 45°$; all wires have a diameter of 2.5 μm and length of 0.5 mm.

of electronic noise (the procedure used follows closely that outlined in Antonia, Satyaprakash & Hussain 1982). The value of f_c was generally close to $U_1/2\pi\eta$, which is commonly identified as the Kolmogorov frequency f_k. The filtered signals were subsequently sampled at a frequency of $f_s \approx 2f_c$ for vorticity measurements and $8f_c$ for the single X-wire measurement into a PC (IBM compatible Pentium 70) using a 12 bit A/D converter. The record duration was 65 s for the former and 210 s for the latter. Yaw and velocity calibrations were also carried out on the PC; the majority of the data processing was done on a VAX 8550 computer.

It is assumed that each X-probe measures two velocity fluctuation components at the centre of the probe. While measured velocity components can be significantly in error when velocity gradients are large (e.g. Vukoslavcevic & Wallace 1981; Kawall, Shokr & Keffer 1983; Hirota, Fujita & Yokosawa 1988; Park & Wallace 1993; Zhu & Antonia 1995), the mean velocity gradient is zero in the present flow. The errors in neglecting the fluctuating instantaneous velocity gradients are estimated (see e.g. Hirota *et al.* 1988) to be about 1 and 3% for u_1' and u_2' (or u_3') respectively using a range of hot-wire yaw factors corresponding to the present experimental conditions. The binormal cooling effect on each X-probe has also been neglected. According to Tutu & Chevray (1975) (see also Camussi *et al.* 1996), neglecting binormal cooling only results in an error of 1–3% for u_1', u_2' (a prime denotes the r.m.s. value) and $\langle u_1 u_2 \rangle$ when the local turbulence intensity is about 10%. The present values of u_i'/U_1 are small ($< 2\%$ for $20 \leqslant x_1/M \leqslant 80$) and therefore the error in neglecting binormal cooling should also be negligible.

The three vorticity components were obtained from the measured u_i of the four X-probes using the following approximation:

$$\omega_1 = u_{3,2} - u_{2,3} \simeq \frac{\Delta u_3}{S_2} - \frac{\Delta u_2}{S_3}, \tag{2.1}$$

$$\omega_2 = u_{1,3} - u_{3,1} \simeq \frac{\Delta u_1}{S_3} + \frac{\Delta u_3}{S_1}, \tag{2.2}$$

$$\omega_3 = u_{2,1} - u_{1,2} \simeq -\frac{\Delta u_2}{S_1} - \frac{\Delta u_1}{S_2}, \tag{2.3}$$

where Δu_3 and Δu_1 in (2.1) and (2.3) respectively are velocity differences between X-probes a and c (figure 1); Δu_2 and Δu_1 in (2.1) and (2.2) respectively are velocity differences between X-probes b and d. Derivatives in the x_1-direction were estimated

using Taylor's hypothesis, i.e. $\partial/\partial x_1 = -U_1\partial/\partial t$. The separation S_1 is identified with $U_1\Delta t$, where Δt ($\simeq f_s^{-1}$) is the time interval between consecutive samples. A forward differencing scheme was used to convert temporal to spatial derivatives with $S_1 \simeq \frac{1}{2}S_2 \simeq \frac{1}{2}S_3$ for $x_1/M \geqslant 40$. While it would have been preferable to use $S_1 \simeq S_2 \simeq S_3$ (Wallace & Foss 1995), S_1 is dictated here by the choice of f_s ($\simeq 2f_k$). Details about the data reduction algorithm of the four-wire (one-component) vorticity probe are given in Antonia *et al.* (1996*b*).

Experimental uncertainties were estimated for all measured quantities. In the case of U_1 and u_i' ($i = 1, 2, 3$), estimates were inferred from errors in the hot-wire calibration data as well as the scatter (20 to 1 odds) observed in repeating the experiment a number of times. The uncertainty for U_1 was about $\pm 2\%$, while uncertainties for u_1', u_2' and u_3' were about $\pm 4.5\%$, $\pm 5\%$ and $\pm 5\%$, respectively. The level of agreement in u_1' from the four X-probes is $\pm 2\%$; u_2' (or u_3') from X-probes b and d (or a and c) also agree within $\pm 2\%$. Uncertainties for wire separations S_i were $\pm 2\%$ ($i = 1$) and $\pm 5\%$ ($i = 2$ and 3). Using the previous estimates, uncertainties for $\langle q^2\rangle$, $\langle \epsilon\rangle$ and $\langle \omega^2\rangle$ were estimated by the method of propagation of errors (e.g. Kline & McClintock 1953; Moffat 1985 1988). The resulting maximum uncertainties for $\langle q^2\rangle$, $\langle \epsilon\rangle$ and $\langle \omega^2\rangle$ were about $\pm 7\%$, $\pm 14\%$ and $\pm 11\%$, respectively. The uncertainties in $\langle \epsilon\rangle$ and $\langle \omega^2\rangle$ were estimated after these two quantities were corrected for the effect of spatial resolution; the magnitudes of the corrections were larger than the uncertainties (see §3), underlining the need to properly account for the effect of systematic errors on velocity derivative data.

3. Corrections due to spatial resolution

Before presenting statistics for u_i or ω_i, it is relevant to address the effect the imperfect spatial resolution of the probe has on the measurements. The high-wavenumber part of the velocity spectrum and, more especially, the vorticity spectrum is expected to be attenuated due to this imperfect resolution. Detailed expressions for this attenuation are given in Antonia *et al.* (1996*b*) for the one-component vorticity probe and Zhu & Antonia (1996) for the three-component vorticity probe. Only a brief outline of the method is presented here; the emphasis is on the attenuation of $\phi_{\omega_i}(k_1)$ or the spectral density of ω_i, defined such that $\int_0^\infty \phi_{\omega_i}(k_1)\mathrm{d}k_1 = \langle \omega_i^2\rangle$ (no summation on i) where k_1 is the wavenumber in the x_1-direction. A measure of this attenuation is given by the ratio

$$R_{\omega_i} = \frac{\phi^m_{\omega_i}(k_1)}{\phi_{\omega_i}(k_1)} = \frac{\displaystyle\int\!\!\int_{-\infty}^{\infty} \phi^m_{\omega_i}(\boldsymbol{k})\mathrm{d}k_2\mathrm{d}k_3}{\displaystyle\int\!\!\int_{-\infty}^{\infty} \phi_{\omega_i}(\boldsymbol{k})\mathrm{d}k_2\mathrm{d}k_3} \tag{3.1}$$

where $\boldsymbol{k}$ is the wavenumber vector with magnitude $k \equiv (k_1^2 + k_2^2 + k_3^2)^{1/2}$, k_2 and k_3 are the wavenumbers in the x_2 and x_3-directions respectively, $\phi^m_{\omega_i}(k_1)$ is the measured spectrum and $\phi_{\omega_i}(k_1)$ is the 'true' or 'correct' spectrum. For each value of i, $\phi_{\omega_i}(\boldsymbol{k})$ can be written in terms of $\phi_{ij}(\boldsymbol{k})$, the energy spectrum tensor. For example, for $i = 2$,

$$\phi_{\omega_2}(\boldsymbol{k}) = \phi_{u_{1,3}}(\boldsymbol{k}) + \phi_{u_{3,1}}(\boldsymbol{k}) - 2Co_{u_{1,3}u_{3,1}}(\boldsymbol{k}) \tag{3.2}$$

and

$$\phi_{u_{i,m}}(\boldsymbol{k}) = k_m^2\phi_{ii}(\boldsymbol{k}), \tag{3.3}$$

$$Co_{u_{i,m}u_{j,m}} = k_m k_n \phi_{ij}(\boldsymbol{k}). \tag{3.4}$$

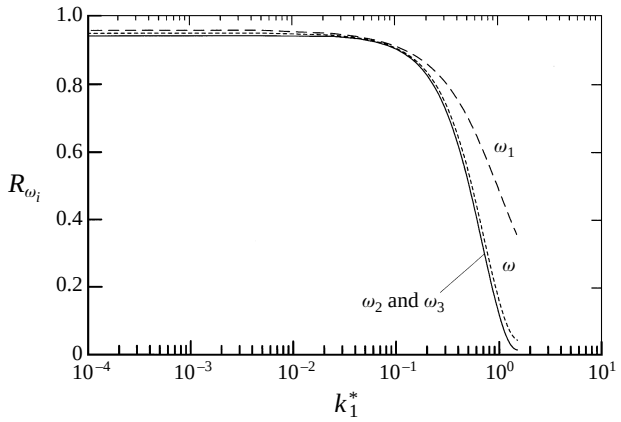

FIGURE 3. Spectral correction ratios for the three-component vorticity probe with a specific choice of geometrical parameters: $S_1^* = S_2^* = S_3^* = 4$; $d_2^* = d_3^* = 2$; $\beta = 45°$; $\ell^* < 1$ (ℓ is the wire length). – –, ω_1; —, ω_2; — - —, ω_3; - - -, ω.

In the case of $\phi^m_{\omega_2}(\boldsymbol{k})$, its components $\phi^m_{u_{1,3}}(\boldsymbol{k})$, $\phi^m_{u_{3,1}}(\boldsymbol{k})$ and $Co^m_{u_{1,3}u_{3,1}}(\boldsymbol{k})$ can also be written in terms of $\phi_{ij}(\boldsymbol{k})$ and all the geometrical parameters of the probe (see (27)–(29) in Zhu & Antonia 1996). To allow the integrals in (3.1) to be evaluated, isotropy is assumed (e.g. Wyngaard 1971) so that

$$\phi_{ij}(\boldsymbol{k}) = \phi_{ij}(k) = \frac{E(k)}{4\pi k^4}(k^2\delta_{ij} - k_i k_j), \tag{3.5}$$

where $E(k)$ is the three-dimensional energy spectrum, here inferred from $\phi_{u_1}(k_1)$ via the isotropic expression

$$E(k) = k^2 \left[\frac{\partial^2 \phi_{u_1}}{\partial k_1^2}\right]_{k_1=k} - k \left[\frac{\partial \phi_{u_1}}{\partial k_1}\right]_{k_1=k}. \tag{3.6}$$

Other possibilities are available for estimating $E(k)$, but the above expression seems optimum since $\phi_{u_1}(k_1)$ can be obtained reliably using a single hot wire of length comparable to η.

It should also be noted that the high-wavenumber part of $\phi_{\omega_i}(k_1)$ ($i = 2$ or 3) is dominated by streamwise derivatives (Antonia *et al.* 1996*b*). Since (3.1) involves integration with respect to k_2 and k_3, the streamwise derivative spectra can be corrected without invoking isotropy or requiring a choice of $E(k)$.

Figure 3 shows the dependence of R_{ω_i} on k_1^* (the superscript * denotes normalization by the Kolmogorov length scale η and the Kolmogorov velocity scale $U_K \equiv \nu^{1/4}\langle\epsilon\rangle^{1/4}$) for a particular choice of probe parameters ($d_2^* = d_3^* = 2$; $S_1^* = S_2^* = S_3^* = 4$; all effective angles are assumed equal to 45° and wire length effects have been neglected). It is clear that ϕ_{ω_1} is much less attenuated (for $k_1^* \gtrsim 0.2$) than ϕ_{ω_2} or ϕ_{ω_3}. The attenuation of ϕ_ω, the sum of the three vorticity spectra, is only slightly smaller than that for ϕ_{ω_2} or ϕ_{ω_3}. For all components, the attenuation remains constant for $k_1^* \lesssim 0.02$. The distributions of R_{ω_i} in figure 3 imply an attenuation of about 20% for $\langle\omega_1^2\rangle$ and about 33% for $\langle\omega_2^2\rangle$ or $\langle\omega_3^2\rangle$.

Relatively convincing support for the above procedure is provided by figure 4. After correction, the ω_3 spectra from the one-component and three-component probes collapse to a good approximation (the uncorrected spectra from the two probes are also shown in figure 4).

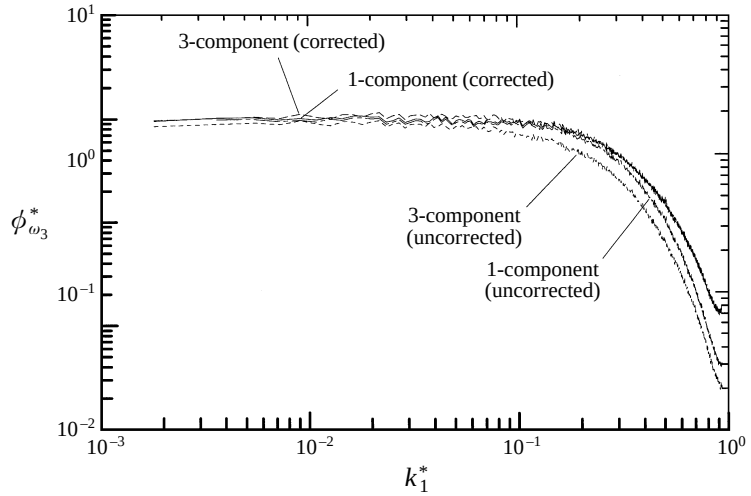

FIGURE 4. Comparison of corrected ω_3 spectra for three-component and one-component vorticity probes. One-component: — - —, uncorrected; —, corrected. Three-component: - - -, uncorrected; – –, corrected. (Here and in subsequent figures, all spectra are for measurements at $x_1/M = 70$.)

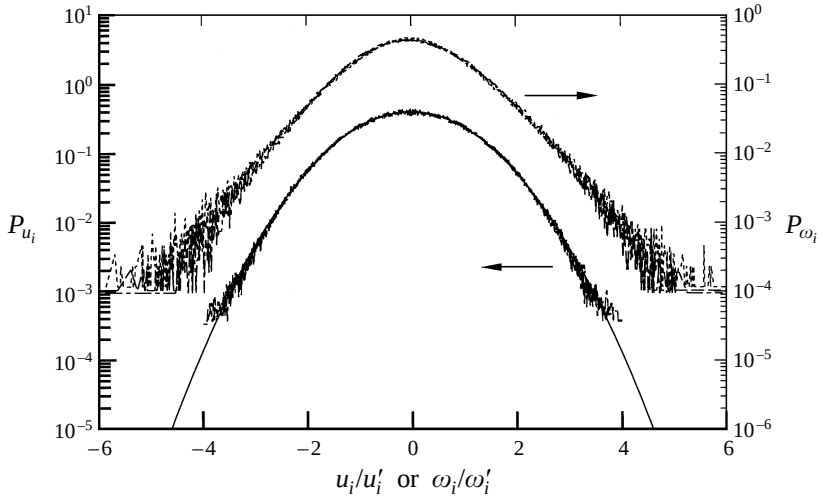

FIGURE 5. Probability density functions of velocity and vorticity fluctuations. — - —, $i = 1$; - - -, 2; – –, 3; —, Gaussian distribution.

4. Statistics of u_i and ω_i

Figure 5 shows the probability density functions (p.d.f.s) of u_i and ω_i. The p.d.f.s of ω_i ($i = 1,2,3$) follow each other remarkably well, as is also the case for the p.d.f.s of u_i. Whereas the p.d.f.s of u_i are almost Gaussian, the p.d.f.s of ω_i are nearly exponential for $|\omega_i/\omega_i'| \geqslant 3$. The near symmetry of the p.d.f.s, of both u_i and ω_i, implies that the skewness is quite small, which is consistent with isotropy.

The present values of $\langle u_1^2 \rangle$, $\langle u_2^2 \rangle$ and $\langle u_3^2 \rangle$ show a clear departure from isotropy, with $\overline{u_3^2}$ about 14% smaller than $\overline{u_1^2}$ and $\overline{u_2^2}$ about 33% smaller than $\overline{u_1^2}$. Comte-Bellot & Corrsin (1966) found that $\overline{u_1^2}$ was about $12 \sim 15\%$ greater than $\overline{u_2^2}$. TKD and Lemonis (1995) reported values of $\langle u_1^2 \rangle$ typically 23% larger than $\langle u_2^2 \rangle$ in the range $30 \leqslant$

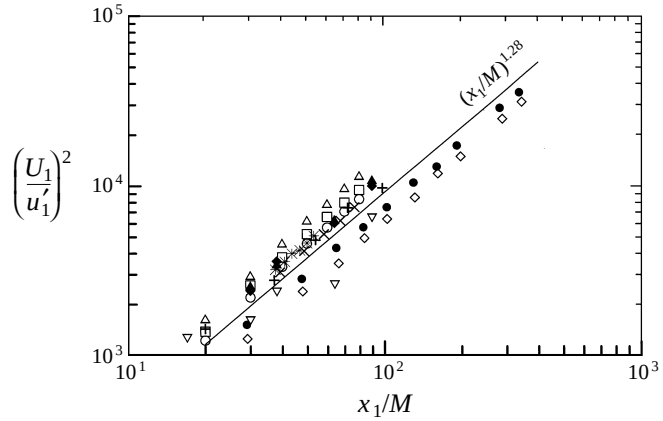

FIGURE 6. Variation of normalized velocity variance $(U_1/u_i')^2$ with x_1/M. Present: ○, $i = 1$; □, 2; △, 3; —, $\sim (x_1/M)^{1.28}$. Comte-Bellot & Corrsin (1966): ◇, $i = 1$; ●, 2. Fan (1991): +, $i = 1$. Mohamed & LaRue (1990): ×, $i = 1$. Van Atta & Chen (1969): *, $i = 1$. TKD: ▽, $i = 1$; ◆, 2; ▲, 3.

$x_1/M \leqslant 90$. In the present experiment, the correlation coefficients $\langle u_1u_2\rangle/\langle u_1^2\rangle^{1/2}\langle u_2^2\rangle^{1/2}$, $\langle u_1u_3\rangle/\langle u_1^2\rangle^{1/2}\langle u_3^2\rangle^{1/2}$, $\langle u_2u_3\rangle/\langle u_2^2\rangle^{1/2}\langle u_3^2\rangle^{1/2}$ were typically –0.017, 0.02 and 0.08. These are sufficiently small to assume that the shear stresses are all equal to zero (consistent with symmetry; isotropy would also require that $\langle u_1u_2\rangle = 0$). They are also smaller than the values (0.10–0.15) quoted by TKD for the first two coefficients.

Figure 6 shows the present distributions of $(U_1/u_i')^2$ as a function of x_1/M. Also shown are the data of Comte-Bellot & Corrsin (1966), Van Atta & Chen (1969), Mohamed & LaRue (1990), Fan (1991) and TKD. The Reynolds number R_M for these studies are 33 900, 25 600, 14 000, 12 800 and 28 000, respectively. Comte-Bellot & Corrsin (1966) noted that

$$\left(\frac{U}{u_i'}\right)^2 \sim \left(\frac{x_1}{M} - \frac{x_0}{M}\right)^n, \tag{4.1}$$

where x_0 is the virtual origin. They also found that the values of x_0 and n differed slightly for each velocity component. However, if x_0 is not subtracted from the data, each data set follows a straight line in the region $x_1/M \geqslant 30$ and these lines have approximately the same power law ($n \simeq 1.28$). The magnitude of n depends normally on the choice of x_0. Mohamed & LaRue (1990) estimated x_0 and n by selecting data only in the range where the ratio $-U_1(\mathrm{d}\langle q^2\rangle/\mathrm{d}x_1)/2\langle\epsilon\rangle$ (with $\langle\epsilon\rangle = \langle\epsilon_{iso}\rangle = 15\nu\langle u_{1,1}^2\rangle$) is nearly 1. This method was also used here for estimating x_0. The present data (see §4) show that the ratio is indeed equal to 1 ($\pm 10\%$) for $x_1/M \geqslant 30$. Using the data in this range and the trial and error method suggested by Comte-Bellot & Corrsin (1966), we estimated that $x_0/M = 3$ and $n = 1.28$. Varying x_0/M by ± 1 results in only a $\pm 3\%$ change in n.

Figure 7 shows spectra of the three velocity components, i.e. $\phi_{u_1}^*$, $\phi_{u_2}^*$ and $\phi_{u_3}^*$ which have been corrected for the effect of spatial resolution of the X-probes and the isotropic calculation of the spectra of lateral components. Because of the solenoidality of u_i in an incompressible flow (Batchelor 1953; Monin & Yaglom 1975; Antonia & Kim 1994), isotropic relations between velocity spectra can be written as

$$\phi_{u_2}^* = \phi_{u_3}^* = \frac{1}{2}\left(1 - k_1^*\frac{\partial}{\partial k_1^*}\right)\phi_{u_1}^*. \tag{4.2}$$

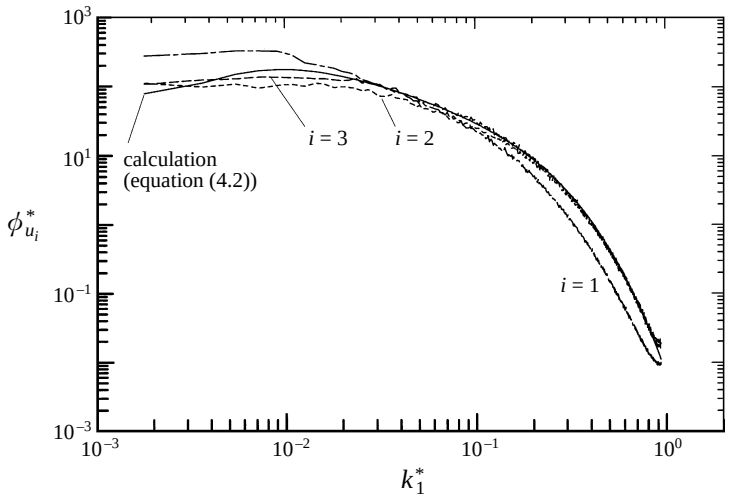

FIGURE 7. Spectra of velocity fluctuations. — - —, $i = 1$; - - -, 2; – –, 3; —, isotropic calculation for $i = 2$ or 3 using (4.2).

There is an analogous relation for the vorticity spectra, since vorticity is solenoidal, independently of whether the flow is incompressible or not. The measured $\phi^*_{u_2}$ and $\phi^*_{u_3}$ distributions show a significant departure from (4.2) at small wavenumbers, reflecting the anisotropy of larger scales. The level of agreement between calculation and measurement for $k_1^* \geqslant 0.1$ is comparable to that shown in figure 3 of TKD.

Uncorrected and corrected spectra of ω_i are shown and compared with isotropic calculations in figure 8. For the isotropic relation, the spectra ϕ_{ω_i} can be written in terms of ϕ_{u_1} or $\phi_{u_{1,1}}$ (e.g. Van Atta 1991; Kim & Antonia 1993)

$$\phi_{\omega_1}(k_1) = \phi_{u_{1,1}}(k_1) + 4\int_{k_1}^{\infty} \frac{\phi_{u_{1,1}}(k)}{k}\mathrm{d}k, \tag{4.3}$$

$$\phi_{\omega_2}(k_1) = \phi_{\omega_3}(k_1) = \frac{5}{2}\phi_{u_{1,1}}(k_1) - \frac{k_1}{2}\frac{\partial\phi_{u_{1,1}}(k_1)}{\partial k_1} + 2\int_{k_1}^{\infty} \frac{\phi_{u_{1,1}}(k)}{k}\mathrm{d}k. \tag{4.4}$$

As already indicated in figure 4, the correction for ϕ_{ω_1} is smaller than that for ϕ_{ω_2} or ϕ_{ω_3}. The distributions of corrected $\phi^*_{\omega_2}$ and $\phi^*_{\omega_3}$ are very close to each other for nearly all values of k_1^*. The agreement between corrected spectra and corresponding isotropic calculations is quite good, reflecting the association of vorticity mainly with small scales.

5. Transport equations for $\langle q^2\rangle$ and $\langle\omega^2\rangle$

The accuracy with which $\langle\epsilon\rangle$ and $\langle\omega^2\rangle$ are estimated by the three-component vorticity probe, can be assessed. For decaying grid turbulence, the transport equation for $\langle q^2\rangle$ simplifies to (e.g. Tennekes & Lumley 1972)

$$U_1\frac{\mathrm{d}\frac{1}{2}\langle q^2\rangle}{\mathrm{d}x_1} + \frac{\mathrm{d}}{\mathrm{d}x_1}\left(\tfrac{1}{2}\langle q^2u_1\rangle\right) + \frac{\mathrm{d}}{\mathrm{d}x_1}(\langle pu_1\rangle) + \langle\epsilon\rangle = 0. \tag{5.1}$$

Only the assumption of homogeneity in the transverse (x_2, x_3)-plane is required for (5.1). Tennekes & Lumley argued that $\mathrm{d}(\langle pu_1\rangle + \frac{1}{2}\langle q^2u_1\rangle)/\mathrm{d}x_1$ is negligible compared

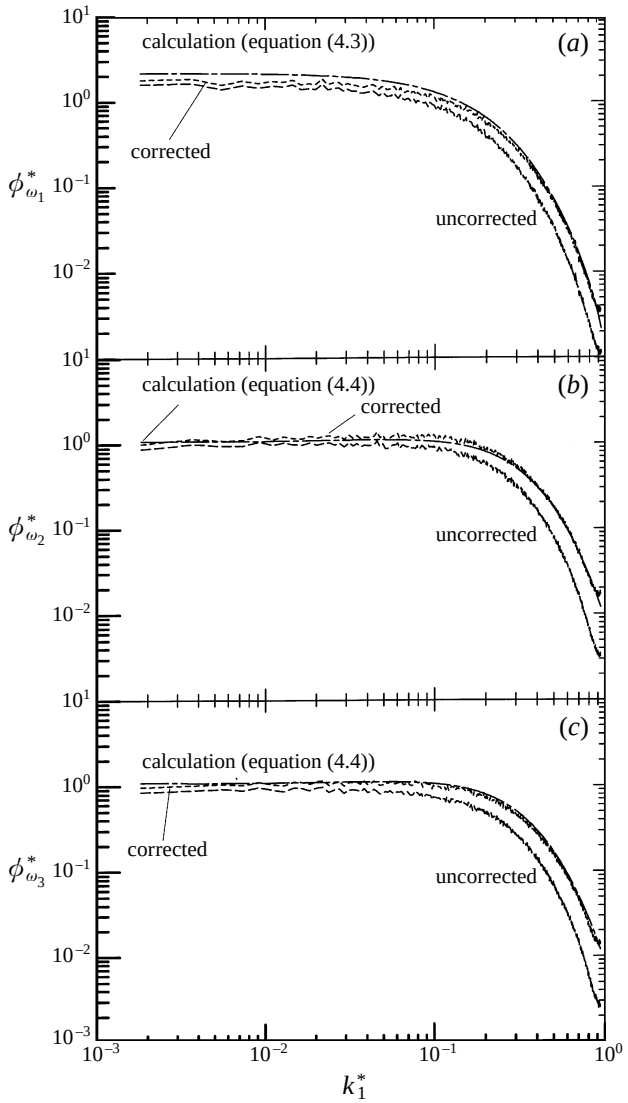

FIGURE 8. Spectra of vorticity fluctuations. – –, Uncorrected; - - -, corrected; — - —, isotropic calculation using (4.3) and (4.4). (*a*) ω_1; (*b*) ω_2; (*c*) ω_3.

with the other terms due to the small velocity fluctuations. Here, $\langle u_1^2\rangle^{1/2}/U_1$ is less than 1% at $x_1/M = 80$; the second term on the left of (5.1) was estimated directly and found to be about 3 orders of magnitude smaller than the first term. Since the third term is likely to be comparable to the second term, it is reasonable to assume that (1.1) is a good approximation to (5.1).

The mean enstrophy $\langle\omega^2\rangle$ is given by

$$\begin{aligned}\langle\omega^2\rangle &= \epsilon_{ijk}\epsilon_{imn}\langle u_{k,j}u_{n,m}\rangle \\ &= \langle u_{1,2}^2\rangle + \langle u_{2,1}^2\rangle + \langle u_{1,3}^2\rangle + \langle u_{3,1}^2\rangle + \langle u_{2,3}^2\rangle + \langle u_{3,2}^2\rangle \\ &\quad - 2\langle u_{1,2}u_{2,1}\rangle - 2\langle u_{1,3}u_{3,1}\rangle - 2\langle u_{2,3}u_{3,2}\rangle. \end{aligned} \tag{5.2}$$

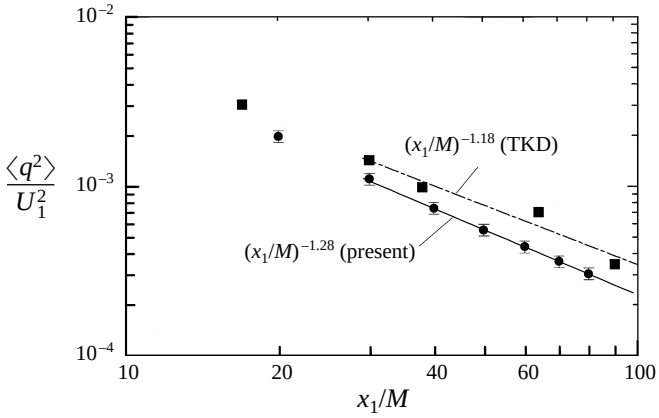

FIGURE 9. Decay of turbulent energy $\langle q^2\rangle/U_1^2$ with x_1/M. ●, Present; ■, estimated from TKD; —, $\sim (x_1/M)^{-1.28}$; — - —, $\sim (x_1/M)^{-1.18}$. Error bars indicate experimental uncertainties.

All of the velocity gradients which appear on the right of (5.2) can be estimated. The homogeneous value of $\langle\epsilon\rangle$ ($\equiv \nu\langle\omega^2\rangle$) can therefore also be obtained.

The full mean dissipation rate $\langle\epsilon\rangle = 2\nu\langle s_{ij}s_{ij}\rangle$, where s_{ij} is the turbulent rate of strain $\frac{1}{2}(u_{i,j} + u_{j,i})$, can be written

$$\langle\epsilon\rangle = \nu\{2\langle u_{1,1}^2\rangle + 2\langle u_{2,2}^2\rangle + 2\langle u_{3,3}^2\rangle + \langle u_{1,2}^2\rangle + \langle u_{2,1}^2\rangle + \langle u_{1,3}^2\rangle + \langle u_{3,1}^2\rangle + \langle u_{2,3}^2\rangle + \langle u_{3,2}^2\rangle + 2\langle u_{1,2}u_{2,1}\rangle + 2\langle u_{1,3}u_{3,1}\rangle + 2\langle u_{2,3}u_{3,2}\rangle\}. \quad (5.3)$$

All terms on the right-hand side of (5.3) can be estimated except for the second and third terms. The quantities $u_{2,2}$ and $u_{3,3}$ are not measured with the present probe; they can however be estimated by assuming incompressibility, namely

$$u_{1,1} + u_{2,2} + u_{3,3} = 0 \quad (5.4)$$

or

$$2\langle u_{2,2}^2\rangle + 2\langle u_{3,3}^2\rangle = 2\langle u_{1,1}^2\rangle - 4\langle u_{2,2}u_{3,3}\rangle. \quad (5.5)$$

Assuming homogeneity, the last term on the right of (5.5) can be replaced by $-4\langle u_{2,3}u_{3,2}\rangle$ since

$$\langle u_{2,2}u_{3,3}\rangle = \langle u_{2,3}u_{3,2}\rangle. \quad (5.6)$$

Substitution of (5.5) and (5.6) into (5.3) then yields

$$\langle\epsilon\rangle = \nu\{4\langle u_{1,1}^2\rangle + \langle u_{1,2}^2\rangle + \langle u_{2,1}^2\rangle + \langle u_{1,3}^2\rangle + \langle u_{3,1}^2\rangle + \langle u_{2,3}^2\rangle + \langle u_{3,2}^2\rangle + 2\langle u_{1,2}u_{2,1}\rangle + 2\langle u_{1,3}u_{3,1}\rangle - 2\langle u_{2,3}u_{3,2}\rangle\}. \quad (5.7)$$

The decay of $\langle q^2\rangle/U_1^2$ with x_1/M, is shown in figure 9. A least-squares fit to the data in the range $x_1/M \geqslant 30$ indicates that $\langle q^2\rangle \sim (x_1/M)^{-1.28}$, an expected result since all the three normal stresses decay as $(x_1/M)^{-1.28}$ (figure 6). The TKD data for $\langle q^2\rangle$ are also included in figure 9; they indicate an exponent of -1.18 (note that the scatter is considerably larger than for the present data).

The values of $\langle\epsilon\rangle$ inferred from (5.7) (all the variances and covariances in this expression were evaluated by integrating the corrected spectra and cospectra) are shown in figure 10. The decay rate of $\langle\epsilon\rangle$, with an exponent of -2.28, is clearly consistent with the decay rate of $\langle q^2\rangle$ (figure 9). The values of $\langle\epsilon\rangle$ should be compared properly with (1.1), i.e. the solid line should represent $-U_1\,\mathrm{d}(\frac{1}{2}\langle q^2\rangle)/\mathrm{d}x_1$. For TKD,

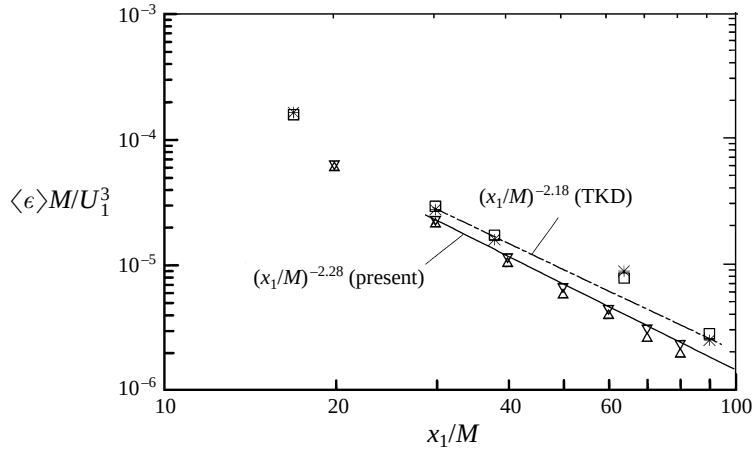

FIGURE 10. Decay of $\langle\epsilon\rangle M/U_1^3$ with x_1/M. Present: $\triangle$, $\langle\epsilon\rangle$; $\triangledown$, $\langle\epsilon_{iso}\rangle$; —, $\sim (x_1/M)^{-2.28}$, left-hand side of (1.1). (Inferred from) TKD: $\square$, $\langle\epsilon\rangle$; *, $\langle\epsilon_{iso}\rangle$; — - —, $\sim (x_1/M)^{-2.18}$, left-hand side of (1.1). (Error bars for $\langle\epsilon\rangle$ are not shown in this figure to avoid crowding.)

$\langle\epsilon\rangle$ at 3 values of x_1/M also lie on the line corresponding to the left-hand side of (1.1) (note that the slope is -2.18); this level of agreement is rather surprising since spatial resolution corrections were not applied to these data. The values of $\langle\epsilon_{iso}\rangle$, shown in figure 10, appear to be in even better agreement with (1.1). Although $\langle\epsilon\rangle \simeq \langle\epsilon_{iso}\rangle$, the individual components of $\langle\epsilon\rangle$ exhibit a departure from isotropy. The ratios plotted in figure 11 should all be equal to 1 (horizontal solid line) if isotropy were satisfied. The variances are generally within $\pm 10\%$ (the dashed horizontal lines correspond to values of 1.1 and 0.9) of their isotropic values; since the deviation can be of either sign, this has a compensating effect in terms of producing a near equality between $\langle\epsilon\rangle$ and $\langle\epsilon_{iso}\rangle$. A similar compensation can be seen in the data of TKD and Lemonis. The covariances in figure 11 show the largest departures from isotropy but their contributions to $\langle\epsilon\rangle$ are smaller than those of the variances.

The quantity $(\omega' M/U_1)^{-1}$ is shown in figure 12 as a function of x_1/M. In the range $30 \leqslant x_1/M \leqslant 80$, its rate of increase is $x_1^{1.14}$, consistent with the $x_1^{-2.28}$ variation of $\langle\epsilon\rangle$. (The TKD data suggest an exponent less than 1, but the scatter of the data is large). Note that $(\omega' M/U_1)^{-1}$ has been multiplied by $R_M^{1/2}$ to allow a more meaningful comparison with the data of TKD and Lemonis which are at slightly different Reynolds numbers. Although self-preservation is expected when $\langle\epsilon\rangle$ is normalized by the relevant scales (for simplicity, M and U_1 are used here, a more rigorous normalization would be based on L, the integral length scale, and u_1', as noted by Sreenivasan 1984), $\langle\epsilon\rangle = \nu\langle\omega^2\rangle$ in homogeneous turbulence and the Reynolds number needs to be taken explicitly into account when examining $\langle\omega^2\rangle$ for self-preservation (e.g. Antonia, Rajagopalan & Zhu 1996*a*). It is also of interest to compare the present data for $(\omega_1' M/U_1)^{-1}$ with the larger body of previously published data for this quantity in the same flow (figure 13). For the present data, the power-law exponent is about 1.14, which is consistent with the $x_1^{-2.28}$ variations of $\langle\epsilon\rangle$. As noted in §1, the data of Kit *et al.* (1988) and Fan (1991) indicate an exponent of 1, which is inconsistent with the measured exponent of 1.27 for the decay of $u_1'^2$ reported by Fan.

Since velocity derivatives receive a larger contribution from the high-wavenumber part of the spectrum than velocity fluctuations, ω_i should provide a better check for

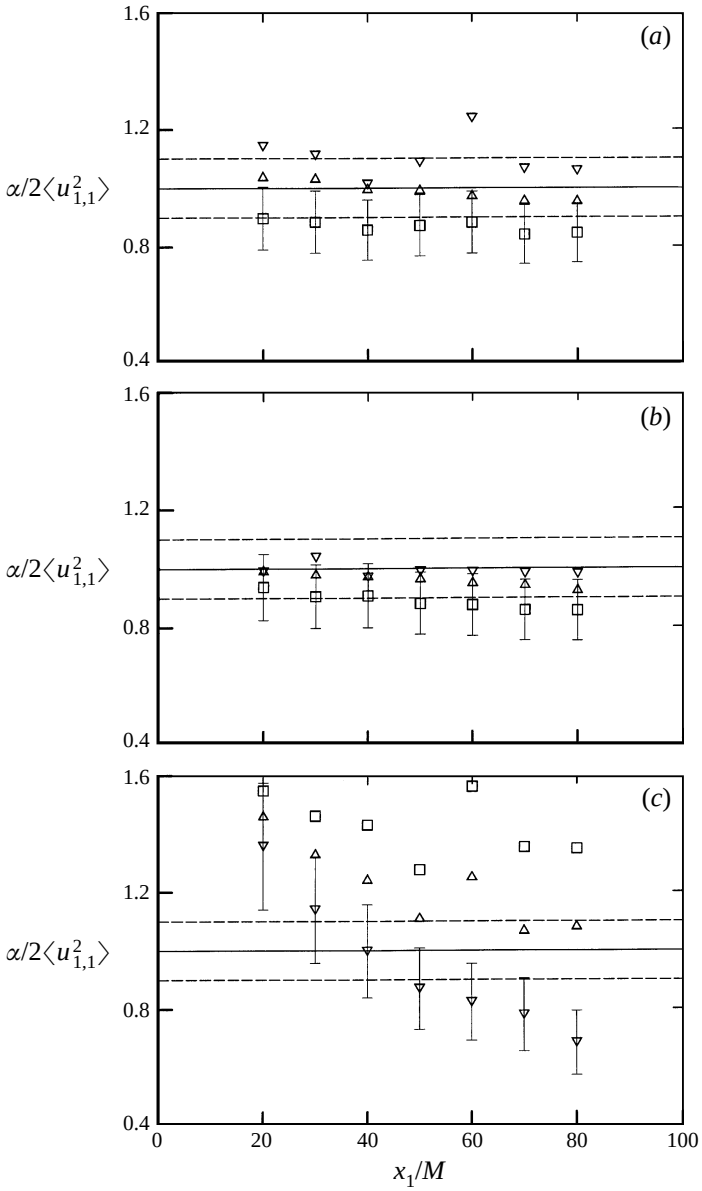

FIGURE 11. Ratios of mean-square values of velocity derivatives; in each case the isotropic value (solid line) is 1. Dashed lines correspond to values of 1.1 and 0.9, i.e. $\pm 10\%$ of isotropic value. (*a*) ∇, $\alpha = \langle u_{1,3}^2 \rangle$; $\square$, $\langle u_{2,1}^2 \rangle$; $\triangle$, $\langle u_{1,2}^2 \rangle$. (*b*) ∇, $\alpha = \langle u_{3,2}^2 \rangle$; $\square$, $\langle u_{2,3}^2 \rangle$; $\triangle$, $\langle u_{3,1}^2 \rangle$. (*c*) ∇, $\alpha = -2\langle u_{1,3}u_{3,1} \rangle$; $\square$, $-2\langle u_{2,3}u_{3,2} \rangle$; $\triangle$, $-2\langle u_{1,2}u_{2,1} \rangle$. Here and in subsequent figures, error bars are shown for one data set only to avoid crowding. Similar uncertainties apply to the other data sets.

local isotropy than u_i. Assuming local isotropy, $\langle \omega_1^2 \rangle = \langle \omega_2^2 \rangle = \langle \omega_3^2 \rangle = 5\langle u_{1,1}^2 \rangle$. Figure 14 shows that this equality is reasonably satisfied for the present data (14*a*) and those of TKD (14*b*), although the latter exhibit relatively large scatter at $x_1/M = 38$ and 64. The slight difference in magnitude of the present vorticity components may be due to the uncertainty ($\pm 11\%$) and the slight departure from local isotropy.

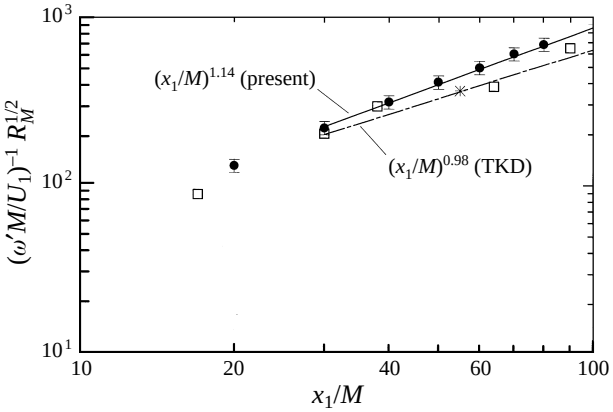

FIGURE 12. Variation of $(\omega' M/U_1)^{-1} R_M^{1/2}$ with x_1/M. ●, Present; □, TKD; ∗, Lemonis (1995); —, $\sim (x_1/M)^{1.14}$; — - —, $\sim (x_1/M)^{0.98}$. Error bars indicate experimental uncertainties.

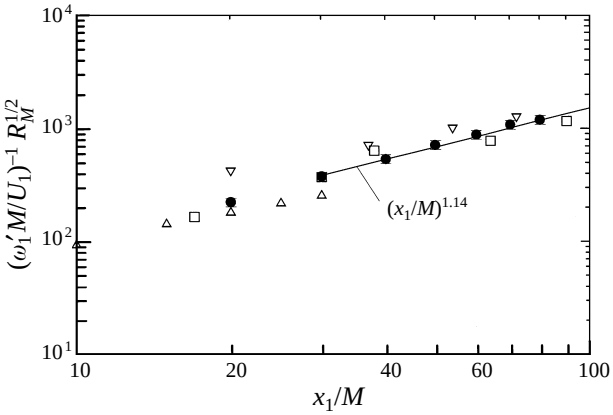

FIGURE 13. Variation of $(\omega_1' M/U_1)^{-1} R_M^{1/2}$ with x_1/M. ●, Present; ▽, Fan (1991); □, TKD. △, Kit *et al.* (1988); —, $\sim (x_1/M)^{1.14}$. Error bars indicate experimental uncertainties.

Equation (1.3) can be rewritten as

$$-U_1 \frac{\mathrm{d}(1/\omega')}{\mathrm{d}x_1} = -\frac{7}{6\sqrt{15}} \left(S + \frac{2G}{R_\lambda} \right). \tag{5.8}$$

The skewness of $u_{1,1}$ is about -0.4 in the range $20 \leqslant x_1/M \leqslant 80$, in close agreement with that reported by BT. The evaluation of G requires $\langle u_{1,11}^2 \rangle$ to be estimated. The latter quantity can be inferred from the spectrum of u_1, via

$$\langle u_{1,11}^2 \rangle = \int_0^\infty k_1^4 \phi_{u_1} \mathrm{d}k_1. \tag{5.9}$$

To obtain satisfactory closure of the integrand $k_1^4 \phi_{u_1}$, the measured distribution of ϕ_{u_1} needs to be extrapolated to higher wavenumbers since the present data stop at $k_1^* \simeq 0.9$. For this purpose, the ϕ_{u_1} data of Comte-Bellot & Corrsin (1971) have been used. There is quite satisfactory agreement between the present measurements and those of Comte-Bellot & Corrsin for $k_1^* \leqslant 0.9$. An eighth-order polynomial fit (with a standard deviation of about ± 0.01) to the present data (on a log-log plot), shown as a dashed line in figure 15, follows the Comte-Bellot & Corrsin data well. The fit was

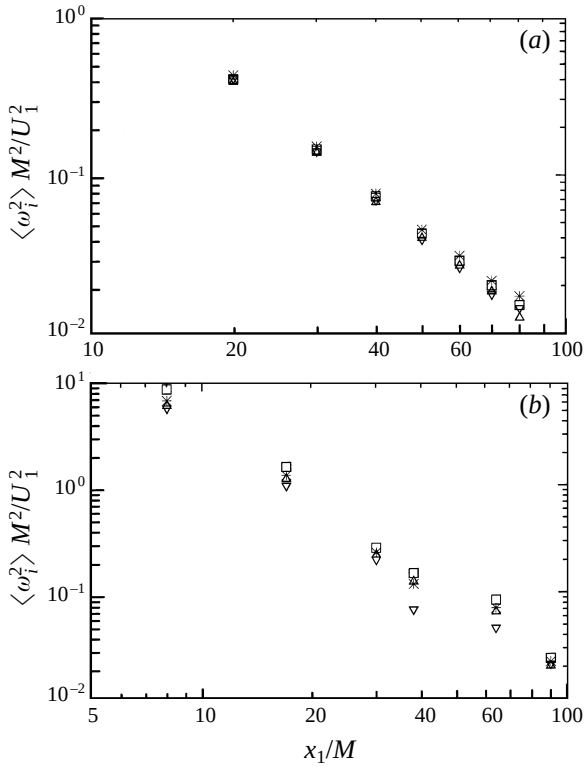

FIGURE 14. Components of mean-square vorticity and comparison with isotropy. ▽, $i = 1$; □, 2; △, 3; ∗, $5\langle u_{1,1}^2 \rangle$. (*a*) Present; (*b*) TKD. (Error bars for $\langle \omega_i^2 \rangle$ are not shown to avoid crowding.)

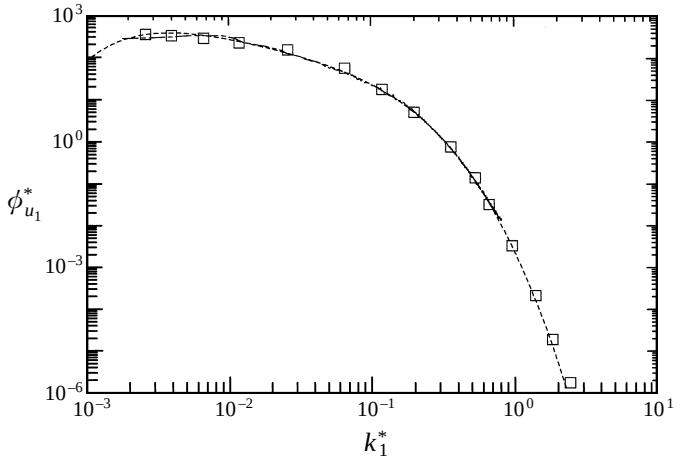

FIGURE 15. u_1 spectrum and comparison with Comte-Bellot & Corrsin (1971). —, Present; □, Comte-Bellot & Corrsin; – –, eighth-order polynomial fit to the present data.

therefore used to extrapolate the present data so as to obtain more reliable estimates of $\langle u_{1,11}^2 \rangle$ (and also $\langle u_{1,1}^2 \rangle$) than if the integration were restricted to $k_1^* \leqslant 0.9$. (The extrapolated portion in figure 15 represents about 2% of the total area under the extrapolated curve.)

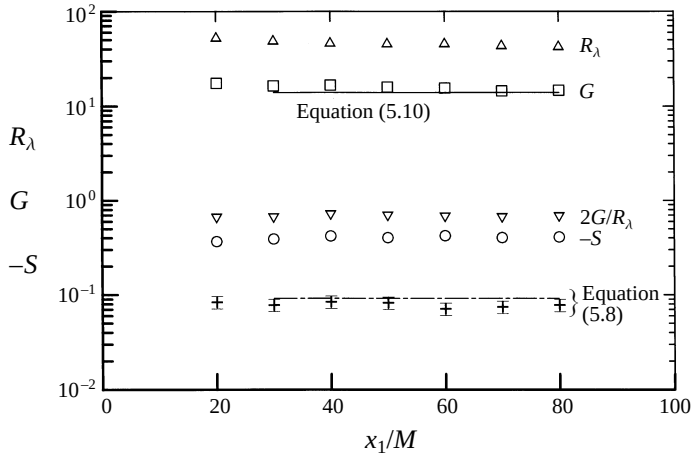

FIGURE 16. Variation of $-S$, G and R_λ with x_1/M and terms in (5.8). ○, $-S$; □, G; △, R_λ; ▽, $2G/R_\lambda$; —, G calculated using (5.10). +, right-hand side of (5.8); — - —, left-hand side of (5.8) inferred from figure 12. Error bars indicate experimental uncertainties.

Figure 16 shows distributions of S, G and R_λ. For isotropic turbulence, these quantities should satisfy the relation

$$G = \frac{27}{7} - \frac{R_\lambda S}{2}, \tag{5.10}$$

where the constant (27/7) on the right-hand side of (5.10) differs from that (30/7) given in BT due to the difference in the decay exponents for $\langle q^2 \rangle$ between the two experiments. While the directly measured values of G depart from the values obtained from (5.10) at small x_1/M, the agreement improves as x_1/M increases.

Justification of (5.8) is also presented in figure 16 by comparing the two sides of this equation. The decay rate of vorticity, i.e. the left-hand side of the equation, was inferred from the slope of the vorticity r.m.s. distribution in figure 12. The right-hand side of (5.8), estimated from the distributions of S, G and R_λ, agrees to within 15% with the decay rate of vorticity; this indicates that experimental data conform reasonably well with the isotropic form of (1.2).

As a further check of isotropy, relatively reliable estimates were made of the mean-square values of $\omega_{i,1}$ ($i = 1, 2, 3$). As for figure 15, eighth-order polynomial fits to the measured ω_i spectra were used to extrapolate the distributions of $k_1^2 \phi_{\omega_i}$ to sufficiently large values of k_1^* to allow the areas under the curves in figure 17 to be calculated more reliably. Since ω_i is inherently solenoidal, isotropy requires that

$$\langle \omega_{2,1}^2 \rangle = \langle \omega_{3,1}^2 \rangle = 2\langle \omega_{1,1}^2 \rangle.$$

The areas under the extrapolated distributions in figure 17 satisfy the above equality within $\pm 10\%$. The extrapolations in figure 17 represent about 4% of the total area for $\langle \omega_{1,1}^2 \rangle$ and about 8% for $\langle \omega_{2,1}^2 \rangle$ and $\langle \omega_{3,1}^2 \rangle$.

6. Global and local statistics of instantaneous enstrophy and energy dissipation rates

We first consider here various global characteristics of ϵ and ω primarily in order to establish the degree of correlation between these quantities. We also assess the extent to which $u_{1,1}^2$ can represent ϵ.

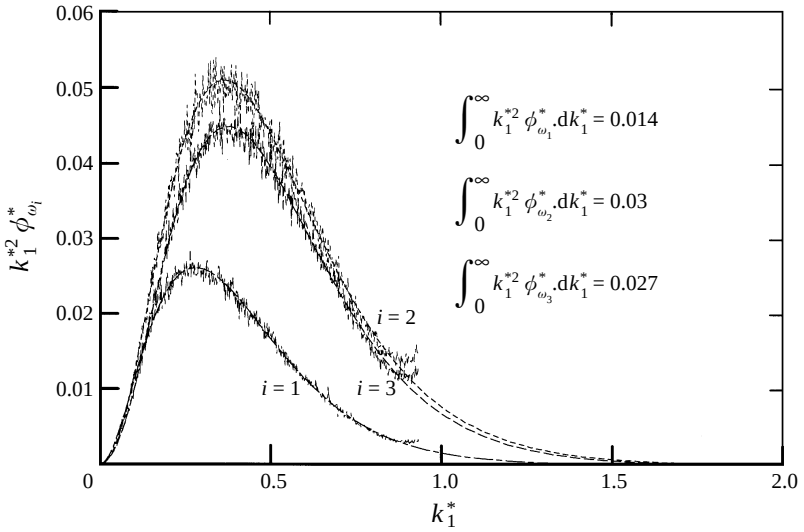

FIGURE 17. Spectra of vorticity (corrected) weighted by k_1^{*2} and their eighth-order polynomial extrapolations. — - —, ω_1; - - -, ω_2; – –, ω_3.

Four spectral densities have been calculated:

$$\phi_\omega(k_1) = \phi_{\omega_1}(k_1) + \phi_{\omega_2}(k_1) + \phi_{\omega_3}(k_1), \tag{6.1}$$

$$\begin{aligned}\phi_\epsilon(k_1) = \nu[&4\phi_{u_{1,1}}(k_1) + \phi_{u_{2,1}}(k_1) + \phi_{u_{3,1}}(k_1) + \phi_{u_{1,2}}(k_1) + \phi_{u_{3,2}}(k_1) + \phi_{u_{1,3}}(k_1)\\ &+ \phi_{u_{2,3}}(k_1) + 2Co_{u_{1,2}u_{2,1}}(k_1) + 2Co_{u_{1,3}u_{3,1}}(k_1) - 2Co_{u_{2,3}u_{3,2}}(k_1)],\end{aligned} \tag{6.2}$$

$$\phi_{\epsilon_{iso}}(k_1) = 15\nu\phi_{u_{1,1}}(k_1), \tag{6.3}$$

$$\begin{aligned}\phi_{\epsilon_{hom}}(k_1) = \nu[&2\phi_{u_{1,1}}(k_1) + \phi_{u_{1,2}}(k_1) + \phi_{u_{2,1}}(k_1) + \phi_{u_{1,3}}(k_1) + \phi_{u_{3,1}}(k_1) + \phi_{u_{2,3}}(k_1)\\ &+ \phi_{u_{3,2}}(k_1) - 2Co_{u_{2,3}u_{3,2}}(k_1)].\end{aligned} \tag{6.4}$$

The areas, from $k_1 = 0$ to $k_1 = \infty$, under these distributions are equal to $\langle\omega^2\rangle$, $\langle\epsilon\rangle$, $\langle\epsilon_{iso}\rangle$ and $\langle\epsilon_{hom}\rangle$ ($\equiv \nu\langle\omega^2\rangle$) respectively. After normalization of the spectral densities and wavenumbers by Kolmogorov scales, the areas are equal to 1.03, 0.96, 1.0 and 1.0.

Although the areas under the curves are nearly equal, the shape of $\phi^*_{\epsilon_{iso}}$ differs significantly from the other three distributions (figure 18). The main departure is at low wavenumbers where the magnitude of $\phi^*_{\epsilon_{iso}}$ increases steadily with k_1^* until it reaches the maximum at $k_1^* \simeq 0.15$. For $k_1^* \gtrsim 0.5$, $\phi^*_{\epsilon_{iso}}$ merges with the other distributions, reflecting the isotropy of small scales. ϕ_ϵ and ϕ_{ω^2} (or $\phi_{\epsilon_{hom}}$, which is not shown) are nearly indistinguishable at all wavenumbers; this observation was also made by Antonia, Browne & Shah (1988) and Zhu & Antonia (1997).

Spectra of the instantaneous signals corresponding to ϵ, ϵ_{hom}, ϵ_{iso} and ω^2 were also computed. The distributions, shown in figure 19, are normalized so that

$$\int_0^\infty \psi_\alpha(k_1)\mathrm{d}k_1 = \frac{\langle\alpha^2\rangle - \langle\alpha\rangle^2}{\sigma_\alpha^2} = 1 \tag{6.5}$$

where α stands for any one of ϵ, ϵ_{hom}, ϵ_{iso} and ω^2, and σ_α is the standard deviation of α relative to its mean value. Note that ψ_ϵ (which is nearly identical to $\psi_{\epsilon_{hom}}$; $\psi_{\epsilon_{hom}}$ is not

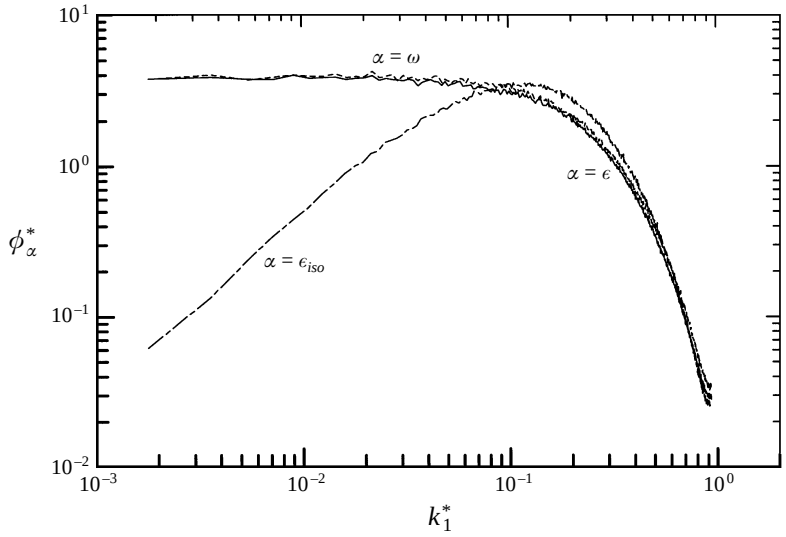

FIGURE 18. Energy dissipation rate and enstrophy spectra. —, $\alpha \equiv \epsilon$; – –, ω; — - —, ϵ_{iso}.

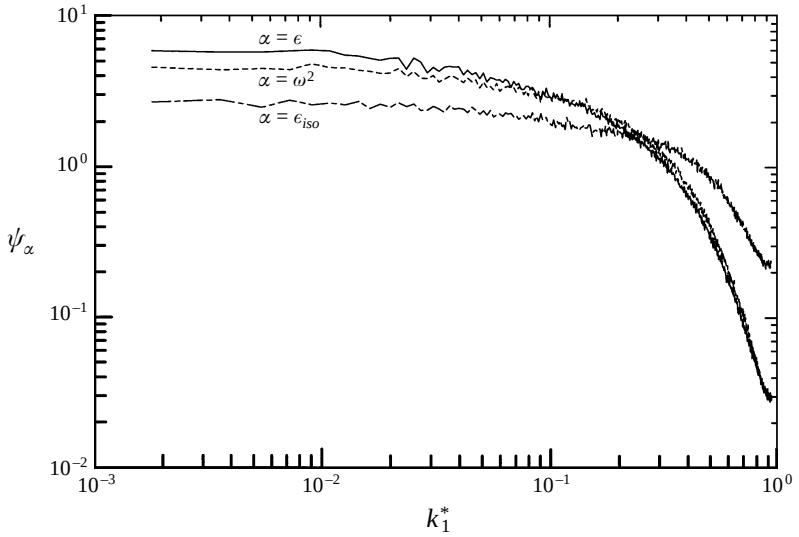

FIGURE 19. Spectra of energy dissipation rate and enstrophy fluctuations. —, $\alpha \equiv \epsilon$; – –, ω^2; — - —, ϵ_{iso}.

shown here) and ψ_{ω^2} do not coincide; they cross over at $k_1^* \simeq 0.1$ before collapsing for $k_1^* \gtrsim 0.5$. The shape of ψ_{iso} differs completely from that of the other two distributions in figure 19, suggesting that $u_{1,1}^2$ is unlikely to be equivalent, on an instantaneous basis, to ϵ.

The p.d.f.s of ϵ and ω^2 are shown in figure 20; the normalization is such that $\int_{-\infty}^{\infty} P_\alpha \mathrm{d}\alpha = 1$, where P_α is the p.d.f. of α. The p.d.f. of ϵ_{hom} differs only very slightly from that of ϵ and has not been included in the figure to avoid confusion. The shape of P_ϵ deviates from that of P_{ω^2} both near zero and at relatively large amplitudes. The positive tails exhibited by P_ϵ and P_{ω^2} are nearly exponential, although the rate of decay is smaller for P_{ω^2} than P_ϵ. This implies that high-order moments of ω^2 will

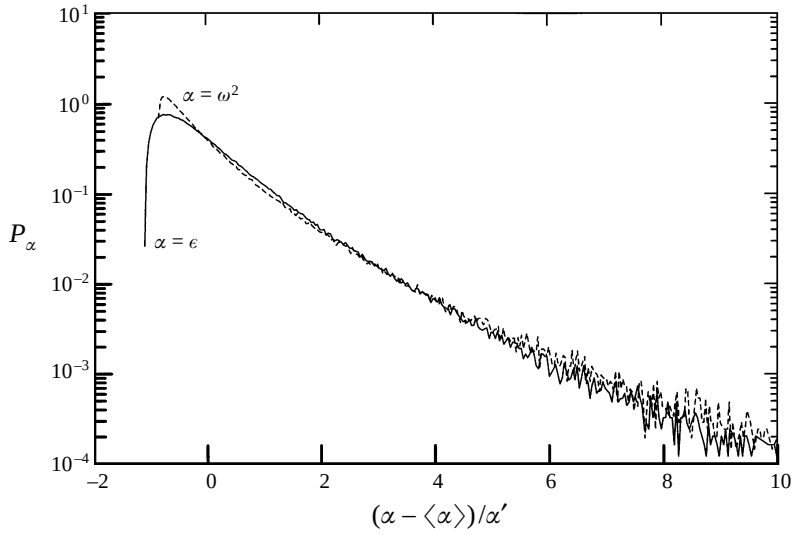

FIGURE 20. Probability density functions of instantaneous energy dissipation rate and enstrophy. —, $\alpha \equiv \epsilon$; – –, ω^2.

be greater than those of ϵ. Indeed, the flatness factor (here, the flatness factor F_α is defined as $F_\alpha = \langle[\alpha - \langle\alpha\rangle]^4\rangle / \langle[\alpha - \langle\alpha\rangle]^2\rangle^2$ where $\alpha = \omega^2$ or ϵ) of ω^2 is 40% higher than that of ϵ.

The amounts of correlation between ϵ and ω^2, ϵ_{iso} and ω^2 and ϵ_{hom} and ω^2 can be inferred from the joint probability density functions (j.p.d.f.) of these quantities (figure 21). The j.p.d.f. $P_{\alpha,\beta}$ (α and $\beta = \omega^2$, ϵ_{hom}, ϵ_{iso} or ϵ) is defined such that $\iint_{-\infty}^{\infty} P_{\alpha,\beta} \mathrm{d}\gamma \cdot \mathrm{d}\delta = 1$, where γ and δ represent centred values of α and β, normalized by their r.m.s. values. Not surprisingly, the correlation between ϵ_{hom} and ω^2 is significant with a coefficient $\rho_{\epsilon_{hom},\omega^2}$ ($\rho_{\alpha,\beta} = \{(\alpha - \langle\alpha\rangle)(\beta - \langle\beta\rangle\}/\alpha'\beta'$) of 0.8 (figure 21*a*). A larger value might have been expected since $\langle\epsilon_{hom}\rangle$ and $\langle\omega^2\rangle$ are equal within $\pm 5\%$, thus approximately satisfying homogeneity; note however that this equality applies to corrected values of $\langle\epsilon_{hom}\rangle$ and $\langle\omega^2\rangle$. It is quite possible that an even higher value of ρ would have been obtained had we been able to correct the instantaneous fluctuations for spatial resolution. The coefficient ρ_{ϵ,ω^2} (figure 20*b*) is 0.6. While this is smaller than $\rho_{\epsilon_{hom},\omega^2}$, it indicates an important correlation between the energy dissipation rate and enstrophy fields. It is pertinent to mention results from direct numerical simulations of homogeneous isotropic turbulence. This information was recently reviewed by Sreenivasan & Antonia (1997) and only brief comments are needed here. There is general agreement that high vorticity intensity occurs in elongated tube-like structures. However, only moderate ϵ regions appear to surround these tubes (e.g. Ruetsch & Maxey 1991), Kida & Ohkitani (1992) noting that ϵ is double-peaked around the tubes. Moderate vorticity intensity tends to be associated with sheet-like structures, but even in this case, ϵ tends to concentrate (perhaps also in sheet-like fashion) in the vicinity of the ω^2 sheets. These observations point to an important, though far from perfect, correlation between ϵ and ω^2; this seems consistent with our measured correlation coefficient. The contours of $P_{\omega^2,\epsilon_{iso}}$ (figure 21*c*) are quite dissimilar to those in figure 21(*a*, *b*). While the latter show a tendency towards alignment along 45°, the former emphasize a lack of correlation at either small or large values (for either quantity); indeed, their appearance resembles that expected for independent variables

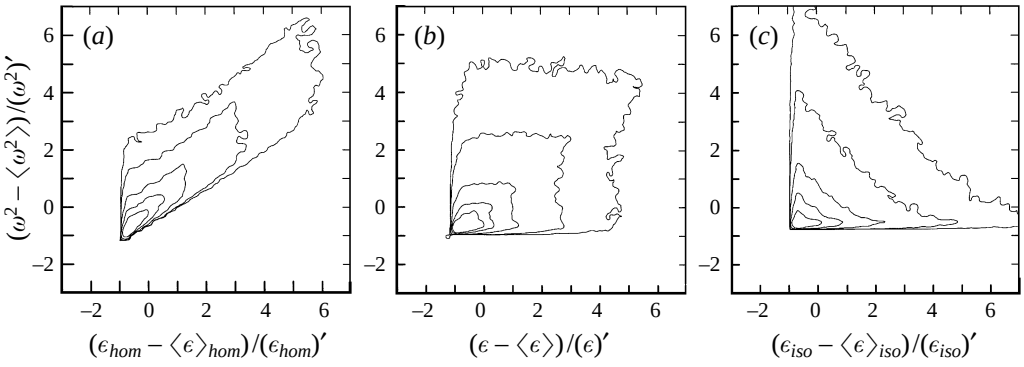

FIGURE 21. Joint probability density functions of ϵ, ϵ_{hom}, ϵ_{iso} and ω^2. (*a*) $P_{\epsilon_{hom},\omega^2}$; (*b*) P_{ϵ,ω^2}; (*c*) $P_{\epsilon_{iso},\omega^2}$. The correlation coefficients $\rho_{\epsilon_{hom},\omega^2}$, ρ_{ϵ,ω^2} and $\rho_{\epsilon_{iso},\omega^2}$ are equal to 0.8, 0.6 and 0.13 respectively. Contour values (outer to inner) 0.0005, 0.005, 0.05, 0.2, 0.6.

(e.g. Tennekes & Lumley 1972; Anselmet & Antonia 1985). Accordingly, $\rho_{\epsilon_{iso},\omega^2}$ is quite small ($\simeq 0.12$), corroborating the expectation that $u_{1,1}^2$ cannot be expected to be instantaneously equivalent to ϵ.

7. Scaling of velocity increments and locally averaged energy dissipation rate and enstrophy

The r-dependence of the moments of δu_1 and δu_2 may provide some insight into the relative importance of ϵ_r and ω_r^2 in determining the scaling behaviour of the longitudinal and transverse velocity increments especially in the context of the DNS based observations (Boratav & Pelz 1997; Chen *et al.* 1997*b*) that δu_2 appears to be more influenced by vorticity whereas δu_1 is dominated by the strain rate. Although the present value of R_λ is too small for an inertial range to occur, an attempt to relate the r-dependencies of $\langle(\delta u_1)^p\rangle$ and $\langle(\delta u_2)^p\rangle$ with those of ϵ_r and ω_r^2 should still be of interest, given the established accuracy of ϵ and ω^2 in the present flow.

Mydlarski & Warhaft (1996, hereafter MW) described grid-generated turbulence for $R_\lambda \lesssim 100$ as weak in the sense that p.d.f.s of δu_1 and δu_2 are nearly Gaussian and dissipation statistics depend only weakly on δu_1 or δu_2 by contrast to observations for $R_\lambda \gtrsim 200$. They also noted that a not particularly well defined scaling range (in the spectra of u_1 and u_2) first appeared at $R_\lambda \simeq 50$.

A relatively good indicator of the scaling range is provided by the behaviour of $\langle(\delta u_1^*)^3\rangle$, namely

$$\langle(\delta u_1^*)^3\rangle = -\tfrac{4}{5}r^*, \tag{7.1}$$

the so-called 'four-fifths law'. The measured values (at $x_1/M = 70$) of the product $C \equiv -\langle(\delta u_1^*)^3\rangle r^{*-1}$ are shown in figure 22. As expected, there is only a very small plateau, centred at $r^* \simeq 20$. The magnitude of C is significantly smaller than 4/5 so that (7.1) is far from being satisfied. The data of MW indicate that C increases with R_λ. The departure from (7.1) reflects a lack of isotropy; note that, here, the normalization does not suffer from the uncertainty normally associated with estimating $\langle\epsilon\rangle$ in non-homogeneous shear flows. Also included in figure 22 is $\langle|\delta u_1^*|^3\rangle$, a quantity used by Benzi *et al.* (1993) in the extended self-similarity (ESS) method for evaluating the exponents of $\langle|\delta u_1|^p\rangle$ over the scaling range. Although there is no theory to describe the behaviour of $\langle|\delta u_1|^3\rangle$, the variation of $\langle|\delta u_1|^3\rangle$ (figure 22) is qualitatively similar

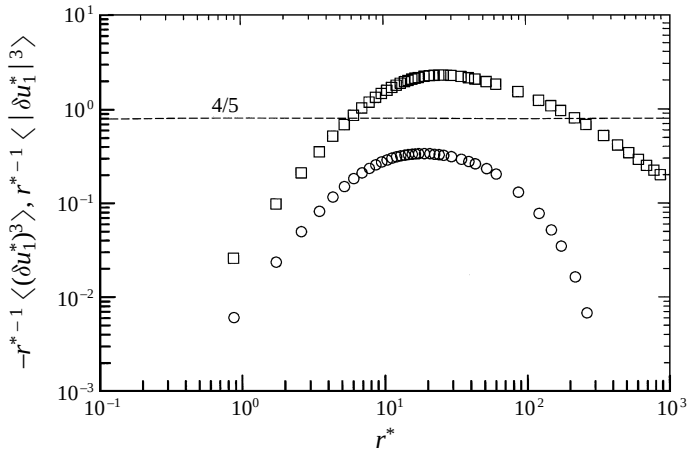

FIGURE 22. Absolute and non-absolute third-order moments of the longitudinal velocity increment, multiplied by r^{*-1}. ○, $-r^{*-1}\langle(\delta u_1^*)^3\rangle$; □, $r^{*-1}\langle|\delta u_1^*|^3\rangle$.

to that of $\langle(\delta u_1)^3\rangle$; the centre of the plateau is slightly displaced ($r^* \simeq 25$) and $C' \equiv -\langle|\delta u_1^*|^3\rangle r^{*-1}$ is equal to about $8C$. The region where $C' \simeq$ const is used here to define the range over which the exponents are evaluated. This constitutes a small but important departure from the way ESS is generally applied. The claim (Benzi *et al.* 1993) that the scaling is extended into the dissipative range becomes tenuous as the magnitude of p increases. This was observed by Stolovitzky & Sreenivasan (1993) and is discernible in the plot of $\log_{10}\langle|\delta u_1^*|^p\rangle$ vs. $\log_{10}\langle|\delta u_1^*|^3\rangle$ of figure 23. It is more emphatic in the case of $\langle|\delta u_2^*|^p\rangle$ (figure 24). The curvature exhibited by the transverse structure functions (figure 24) is not an artefact of the record duration, which was sufficiently long (about 1.5×10^5 integral time scales) to ensure that the integrands $|\delta u_i|^p P_{|\delta u_i|}$ (where $P_{|\delta u_i|}$ is the p.d.f. of $|\delta u_i|$ with $i = 1$, 2 or 3) converged for $p = 8$, the largest value considered here. It represents a genuine departure from the relatively linear behaviour exhibited (figure 23) by the longitudinal increments. The scaling exponents ζ_{u_1} and ζ_{u_2} for the longitudinal and transverse velocity increments respectively were estimated from least-squares regressions over the range ($C' \simeq$ const) indicated by the arrowed horizontal line; for these fits, r^2 always exceeded 0.999 although the standard deviation associated with the value of the exponent increased with p (for $p = 8$, the deviation was equal to $\pm 0.8\%$ for ζ_{u_1} and $\pm 1.0\%$ for ζ_{u_2}). Figure 25 clearly shows that ζ_{u_2} is appreciably smaller than ζ_{u_1}, the difference between these exponents increasing with p. The values of ζ_{u_1} were in excellent agreement with those (not shown here) obtained from a single wire; also the values of ζ_{u_2} were identical to those of ζ_{u_3} (not shown here). The departure from predictions of Kolmogorov (1941, hereafter K41) of ζ_{u_1} is similar to that reported previously for ζ_{u_1} over a range of flows and Reynolds numbers (e.g. Anselmet *et al.* 1984; Frisch 1995; Arneodo *et al.* 1996; Sreenivasan & Antonia 1997) and seems to be adequately represented, at least for $p \leqslant 8$, by either the log-normal (Kolmogorov 1962, hereafter K62) model or the She & Leveque (1994, hereafter SL) model.

Several suggestions have been put forward to explain the inequality $\zeta_{u_2} < \zeta_{u_1}$, which implies that transverse velocity increments are more intermittent than longitudinal velocity increments. Boratav & Pelz (1997) concluded that the inequality mainly reflects the greater contribution to intermittency from enstrophy-dominated structures than from strain-dominated structures. Chen *et al.* (1997*b*) proposed a modification

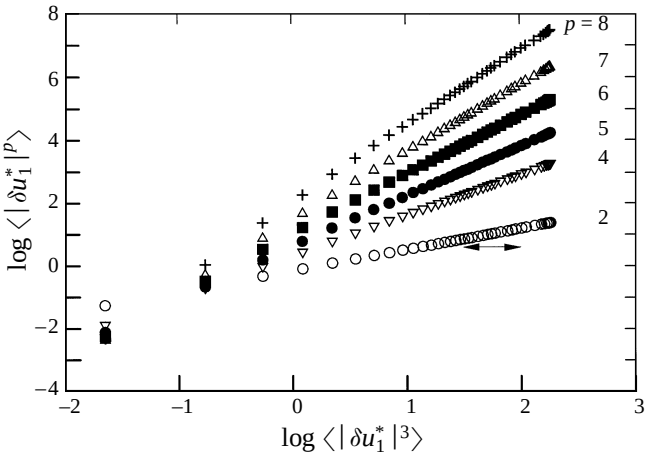

FIGURE 23. $\log\langle|\delta u_1^*|^p\rangle$ vs. $\log\langle|\delta u_1^*|^3\rangle$ for $p = 2$ to 8. Arrowed horizontal line indicates extent of the scaling range.

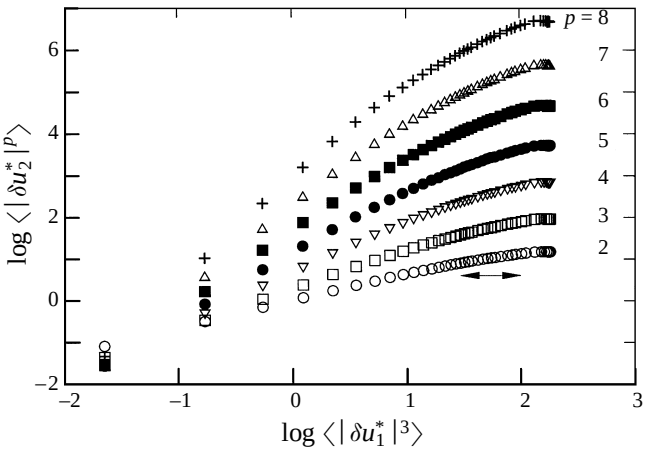

FIGURE 24. $\log\langle|\delta u_2^*|^p\rangle$ vs. $\log\langle|\delta u_1^*|^3\rangle$ for $p = 2$ to 8. Arrowed horizontal line indicates extent of the scaling range.

to the refined similarity hypothesis (RSH) K62, which they called RSHT, in order to relate transverse velocity increments to the enstrophy field. RSH is retained as the link between longitudinal velocity increments and ϵ_r. These authors found that RSH and RSHT were well supported by their DNS data. They also suggested that RSH and RSHT may be treated as independent hypotheses leading to independent and possibly different scaling exponents. It seems appropriate to consider whether RSH and RSHT can explain the present differences between ζ_{u_1} and ζ_{u_2}. RSH and RSHT imply that $\delta u_1 \sim (r\epsilon_r)^{1/3}$ and $\delta u_2 \sim (r\omega_r^2)^{1/3}$ respectively. Assuming that $\langle(\delta u_1)^p\rangle$ and $\langle(\delta u_2)^p\rangle$ scale as $r^{\zeta^L(p)}$ and $r^{\zeta^T(p)}$ in the inertial range, while $\langle\epsilon_r^p\rangle$ and $\langle(\omega_r^2)^p\rangle$ scale as $r^{\tau^d(p)}$ and $r^{\tau^v(p)}$ respectively, we can write

$$\zeta^L(p) = \tfrac{1}{3}p + \tau^d(\tfrac{1}{3}p), \tag{7.2}$$

and

$$\zeta^T(p) = \tfrac{1}{3}p + \tau^v(\tfrac{1}{3}p). \tag{7.3}$$

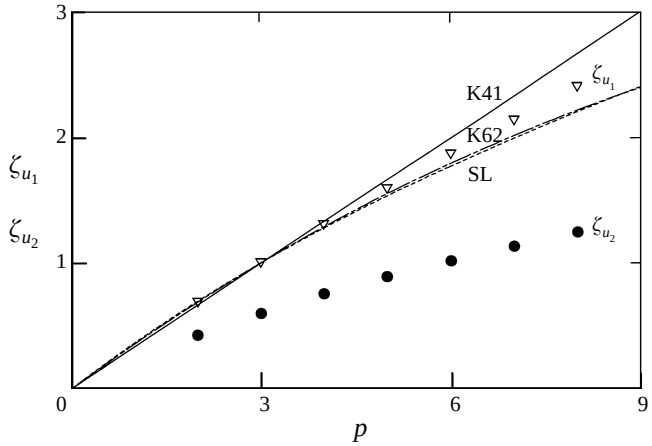

FIGURE 25. Scaling exponents for δu_1 and δu_2. ∇, ζ_{u_1}, estimated from the data in figure 23; ●, ζ_{u_2}, estimated from the data in figure 24; —, K41; – –, SL; — - —, K62.

p	$\tau^d(\frac{1}{3}p)$	$\tau^v(\frac{1}{3}p)$	ζ^L	ζ_{u_1}	ζ^T	ζ_{u_2}
2	$+0.012$ ($\pm 4.8\times10^{-4}$)	$+0.019$ ($\pm 3.9\times10^{-4}$)	0.678	0.683	0.686	0.423
3	-0.005 ($\pm 6.2\times10^{-4}$)	-0.009 ($\pm 5.6\times10^{-4}$)	0.994	1.0	0.992	0.597
4	-0.040 ($\pm 7.1\times10^{-4}$)	-0.061 ($\pm 7.0\times10^{-4}$)	1.293	1.303	1.272	0.752
5	-0.091 ($\pm 7.8\times10^{-4}$)	-0.136 ($\pm 8.2\times10^{-4}$)	1.576	1.592	1.531	0.892
6	-0.158 ($\pm 8.3\times10^{-4}$)	-0.231 ($\pm 9.2\times10^{-4}$)	1.842	1.871	1.769	1.020
7	-0.241 ($\pm 8.7\times10^{-4}$)	-0.347 ($\pm 1.0\times10^{-3}$)	2.092	2.141	1.986	1.137
8	-0.340 ($\pm 9.2\times10^{-4}$)	-0.480 ($\pm 1.0\times10^{-3}$)	2.327	2.405	2.187	1.245

TABLE 1. Longitudinal and transverse scaling exponents

The superscripts L and T have been introduced because the magnitudes of $\zeta^L(p)$ and $\zeta^T(p)$ need not, in general, be the same as those estimated from the ESS. The exponents τ^d and τ^v were inferred from the variations of $\langle \epsilon_r^p \rangle$ (figure 26*a*) and $\langle (\omega_r^2)^p \rangle$ (figure 26*b*) with r over the same range (indicated in the figures) as that used to estimate ζ_{u_1} and ζ_{u_2}. The values of $\tau^d(\frac{1}{3}p)$ and $\tau^v(\frac{1}{3}p)$ are given in table 1, the numbers inside the brackets representing the corresponding standard deviations.

Also shown in table 1 are the values of ζ^L and ζ^T estimated using (7.2) and (7.3) as well as the values of ζ_{u_1} and ζ_{u_2} (previously given in figure 25). For $p > 3$, ζ^T is smaller than ζ^L (the difference is 6.4% for $p = 8$). Arguably, this trend may reflect the more intermittent nature of ω_r^2 relative to that of ϵ_r. Some support for this is provided by figure 27, the flatness factor of ω_r^2 remaining larger than that of ϵ_r. Similar behaviour of $F_{\omega_r^2}$ and F_{ϵ_r} was also found by Chen *et al.* (1997*a*). Note also that in the range $r^* \leqslant 20$, the flatness factor of δu_2 exceeds that of δu_1. However, over the scaling range, $F_{\delta_{u_1}} \simeq F_{\delta_{u_2}}$. For the simulation of Chen *et al.* (1997*b*), $F_{\delta_{u_2}}$ remains slightly larger than $F_{\delta_{u_1}}$ throughout the inertial range. MW reported a nearly perfect equality between $F_{\delta_{u_2}}$ and $F_{\delta_{u_1}}$ for a value of r within the inertial range and for R_λ in the range 50–473.

While $\zeta_{u_1} \simeq \zeta^L$ (table 1), ζ_{u_2} is significantly smaller than ζ^T for all p. It is unlikely that this discrepancy can be attributed, at least for the present small Reynolds number, to the different degrees of intermittency of ϵ_r and ω_r^2. A more likely source of the

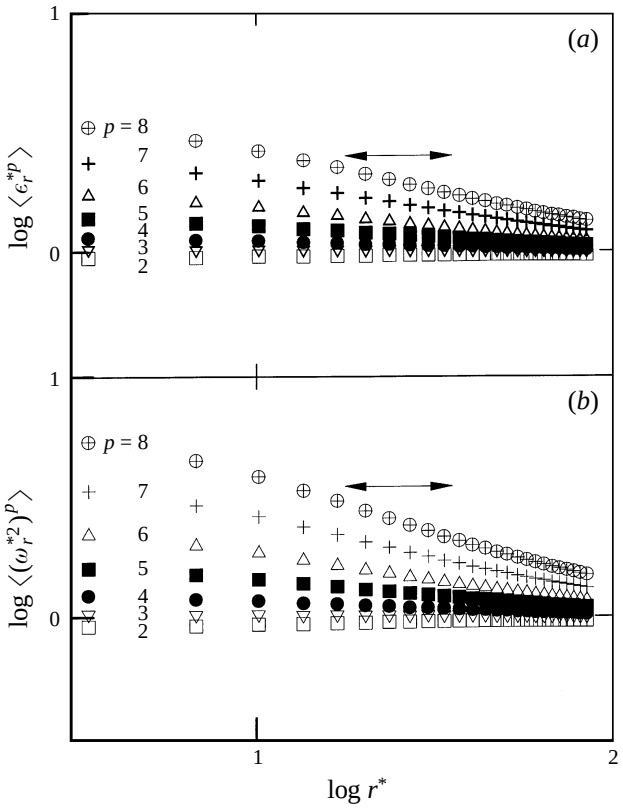

FIGURE 26. Moments of locally averaged energy dissipation rate and enstrophy fluctuations. (*a*) $\langle \epsilon_r^p \rangle$; (*b*) $\langle (\omega_r^2)^p \rangle$.

discrepancy may be that, for this small value of R_λ, any anisotropy in the flow will tend to affect δu_2 more than δu_1. As noted by others (e.g. Herweijer & van de Water 1995), $\zeta_{u_1}(2)$ and $\zeta_{u_2}(2)$ should strictly be equal for homogeneous isotropic turbulence since

$$\langle (\delta u_2)^2 \rangle = \left(1 + \frac{r}{2}\frac{\partial}{\partial r}\right) \langle (\delta u_1)^2 \rangle. \tag{7.4}$$

For the DNS data of Boratav & Pelz (1997) and Chen *et al.* (1997*b*), $\zeta_{u_1}(2) \simeq \zeta_{u_2}(2)$, even though R_λ is not especially large (82 for the former and 216 for the latter), and (7.1) is much more closely satisfied than in the present experiment, apparently reflecting the good isotropy achieved in the simulation. Equation (7.4) was used to calculate $\langle (\delta u_2)^2 \rangle$ from measured $\langle (\delta u_1)^2 \rangle$ data. ESS was then applied, as outlined earlier in this section, to the calculated data; this resulted in an increase in $\zeta_{u_2}(2)$ from 0.42 to 0.50. While the new value of $\zeta_{u_2}(2)$ is closer to the measured value of $\zeta_{u_1}(2)$ than the original estimate, the shortfall remains significant. Possibly a better indicator of isotropy in the inertial range is the magnitude of $C \equiv \langle (\delta u_1^*)^3 \rangle r^{*-1}$, in particular its proximity to 4/5, the constant in (7.1). The present values of C and those of MW ($50 \leqslant R_\lambda \leqslant 473$) suggest that C approaches 0.8 slowly and would reach it only when R_λ approaches 1000. Speculatively, the difference between ζ_{u_1} and ζ_{u_2} should disappear when this occurs. It would seem that available data (e.g. Sreenivasan 1996; MW) for inertial-range constants associated with the spectra of u_1 and u_2 provide

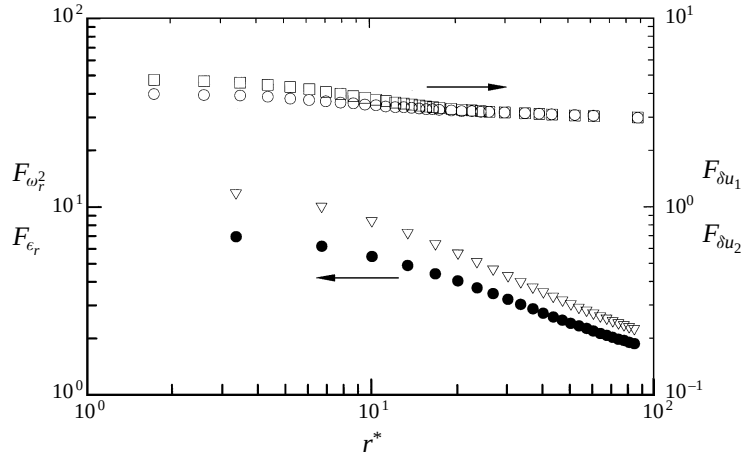

FIGURE 27. Flatness factors of longitudinal and lateral velocity increments and of locally averaged energy dissipation rate and enstrophy. $F_\beta = \langle\beta^4\rangle/\langle\beta^2\rangle^2$ (note that non-centred quantities are used in this definition). ○, $\beta \equiv \delta u_1$; □, δu_2; ●, ϵ_r; ▽, ω_r^2.

some support for this conjecture. Further support is provided by the atmospheric surface layer results of Dhruva *et al.* (1997).

8. Conclusions

The main conclusions of this paper can be summarized as follows.

The data obtained with a relatively simple four-X-wire vorticity probe in decaying grid turbulence indicate that the probe performs satisfactorily in terms of its ability to measure the mean turbulent energy dissipation rate and mean enstrophy reliably. Satisfactory agreement (10%) between the measured values of $\langle\epsilon\rangle$ or $\langle\omega^2\rangle$ and those inferred from the mean turbulent energy decay rate was achieved after correcting the measured derivative spectra for the spatial resolution of the probe.

Although $\langle\epsilon\rangle \simeq \langle\epsilon_{iso}\rangle$, the components of $\langle\epsilon\rangle$ exhibit a non-negligible departure from isotropy. Both $\langle\omega^2\rangle$ and its three components appear to satisfy isotropy approximately. Three of the measured components of the palinstrophy satisfy isotropy within $\pm 10\%$.

Joint p.d.f.s of ϵ_{iso} and ϵ with ω^2 as well as the spectra associated with these quantities indicate that ϵ_{iso} is an inadequate substitute for ϵ.

The joint p.d.f. of ϵ and ω^2 suggests a reasonably high correlation between these quantities. The magnitude of the correlation coefficient ($\simeq 0.6$) seems consistent with evidence from direct numerical simulations of homogeneous isotropic turbulence that regions of strong vorticity do not quite coincide with high energy dissipation rate regions.

Over a range where $\langle|\delta u_1|^3\rangle$ varies linearly with r, the transverse exponents are appreciably smaller than the longitudinal exponents for all values (2 to 8) of p, the moment order. The inequality is larger than that which has been reported, for higher values of R_λ, from either grid turbulence experiments or simulations of forced homogeneous isotropic turbulence.

The present inequality $\zeta_{u_2} < \zeta_{u_1}$ is not satisfactorily accounted for by RSHT, the refined similarity hypothesis for transverse increments proposed by Chen *et al.* (1997*b*), since the measured moments of ϵ_r and ω_r^2 exhibit only slightly different power-law exponents over the scaling range. This slight difference seems commensurate with the

approximate equality between the flatness factors of δu_1 and δu_2 in this range but contrasts with the discernible difference between the flatness factors of ϵ_r and ω_r^2.

Another source for the inequality $\zeta_{u_2} < \zeta_{u_1}$ is the strong scaling-range anisotropy, which reflects the small R_λ of the flow. As R_λ increases and/or the isotropy improves, it is expected that the inequality will eventually disappear for shearless turbulence.

The support of the Australian Research Council is gratefully acknowledged. We are also grateful to Mr B. R. Pearson for his assistance with programming.

REFERENCES

Anselmet, F. & Antonia, R. A. 1985 Joint statistics between temperature and its dissipation in a turbulent jet. *Phys. Fluids* **28**, 1048–1051.

Anselmet, F., Gagne, Y., Hopfinger, E. J. & Antonia, R. A. 1984 High-order velocity structure functions in turbulent shear flows. *J. Fluid Mech.* **140**, 63–89.

Antonia, R. A., Browne, L. W. B. & Shah, D. H. 1988 Characteristics of vorticity fluctuations in a turbulent wake. *J. Fluid Mech.* **189**, 349–365.

Antonia, R. A. & Kim, J. 1994 A numerical study of local isotropy of turbulence. *Phys. Fluids* A **6**, 834–841.

Antonia, R. A. & Pearson, B. R. 1997 Scaling exponents for turbulent velocity and temperature increments. *Europhys. Lett.* **40**, 123–128.

Antonia, R. A., Rajagopalan, S. & Zhu, Y. 1996*a* Scaling of mean square vorticity in turbulent flows. *Expts. Fluids* **20**, 393–394.

Antonia, R. A., Satyaprakash, B. R. & Hussain, A. K. M. F. 1982 Statistics of fine scale velocity in turbulent plane and circular jet. *J. Fluid Mech.* **119**, 55–89.

Antonia, R. A., Zhu, Y. & Shafi, H. S. 1996*b* Lateral vorticity measurements in a turbulent wake. *J. Fluid Mech.* **323**, 173–200.

Arneodo, A., Baudet, C., Belin, F. *et al.* 1996 Structure functions in turbulence, in various flow configurations, at Reynolds number between 30 and 5000, using extended self-similarity. *Europhys. Lett.* **34**, 411–416.

Batchelor, G. K. 1953 *The Theory of Homogeneous Turbulence*. Cambridge University Press.

Batchelor, G. K. & Townsend, A. A. 1947 Decay of vorticity in isotropic turbulence. *Proc. R. Soc. Lond.* A **190**, 534–550 (referred to herein as BT).

Batchelor, G. K. & Townsend, A. A. 1948 Decay of isotropic turbulence in the initial period. *Proc. R. Soc. Lond.* A **193**, 539–558.

Benzi, R., Ciliberto, S., Tripiccione, R., Baudet, C., Massaioli, F. & Succi, S. 1993 Extended self-similarity in turbulent flows. *Phys. Rev.* E **48**, R29–R32.

Boratav, O. N. 1997 On longitudinal and lateral moment hierarchy in turbulence. *Phys. Fluids* **9**, 3120–3122.

Boratav, O. N. & Pelz, R. B. 1997 Structures and structure functions in the inertial range of turbulence. *Phys. Fluids* **9**, 1400–1415.

Camussi, R., Barbagallo, D., Guj, G. & Stella, F. 1996 Transverse and longitudinal scaling laws in non-homogeneous low *Re* turbulence. *Phys. Fluids* **8**, 1181–1191.

Camussi, R. & Benzi, R. 1997 Hierarchy of transverse structure functions. *Phys. Fluids* **9**, 257–259.

Chen, S., Sreenivasan, K. R. & Nelkin, M. 1997*a* Inertial range scalings of dissipation and enstrophy in isotropic turbulence. *Phys. Rev. Lett.* **79**, 1253–1256.

Chen, S., Sreenivasan, K. R., Nelkin, M. & CAO, N. 1997*b* A refined similarity hypothesis for transverse structure functions. *Phys. Rev. Lett.* **79**, 1253.

Comte-Bellot, G. & Corrsin, S. 1966 The use of a contraction to improve the isotropy of grid-generated turbulence. *J. Fluid Mech.* **25**, 657–682.

Comte-Bellot, G. & Corrsin, S. 1971 Simple Eulerian time correlation of full- and narrow-band velocity signals in grid-generated, 'isotropic' turbulence. *J. Fluid Mech.* **48**, 273–337.

Corrsin, S. & Kistler, A. L. 1954 The free-stream boundaries of turbulent flows. *NACA TN* 3133.

Dhruva, B., Tsuji, Y. & Sreenivasan, K. R. 1997 Transverse structure functions in high-Reynolds-number turbulence. *Phys. Rev.* E **56**, R4928–R4930.

Fan, M. 1991 Features of vorticity in fully turbulent flows. PhD Thesis, Yale University.

Foss, J. F. & Haw, R. C. 1990 Transverse vorticity measurements using a compact array of four sensors. In *Symposium on Thermal Anemometry* (ed. D. E. Stock, S. A. Sherif & A. J. Smits). ASME-FED Vol. 97, pp. 71–76.

Frisch, U. 1995 *Turbulence, The Legacy of A. N. Kolmogorov*. Cambridge University Press.

Grossman, S., Lohse, D. & Reeh, A. 1997 Different intermittency for longitudinal and transversal turbulent fluctuations, *Phys. Fluids* **9**, 3817–3825.

Herweijer, J. A. & Water, W. van de 1995 Transverse structure functions of turbulence. In *Advances in Turbulence V* (ed. R. Benzi), pp. 210–216. Kluwer.

Hirota, M., Fujita, H. & Yokosawa, H. 1988 Influences of velocity gradient on hot-wire anemometry with an X-wire probe. *J. Phys.* E: *Sci. Instrum.* **21**, 1077–1084.

Jimenez, J., Wray, A., Saffman, P. G. & Rogallo, R. S. 1993 The structure of intense vorticity in isotropic turbulence. *J. Fluid Mech.* **255**, 65–90.

Kahalerras, H. 1997 Etude experimentale de la profondeur de la cascade de l'intermittence. PhD Thesis, Université Joseph Fourier, Grenoble.

Kahalerras, H., Malecot, Y. & Gagne, Y. 1996 Transverse velocity structure functions in developed turbulence. In *Advances in Turbulence VI* (ed. S. Gavrilakis, L. Machiels & P. A. Monkewitz), pp. 235–238. Kluwer.

Kármán, T. von 1937 The fundamentals of the statistical theory of turbulence. *J. Aero. Sci.* **4**, 131–138.

Kármán, T. von & Howarth, L. 1938 On the statistical theory of isotropic turbulence. *Proc. R. Soc. Lond.* A **164**, 192–215.

Kawall, J. G., Shokr, M. & Keffer, J. F. 1983 A digital technique for the simultaneous measurement of streamwise and lateral velocities in turbulent flows. *J. Fluid Mech.* **133**, 83–112.

Kerr, R. M. 1985 High-order derivative correlations and the alignments of small-scale structures in isotropic numerical turbulence. *J. Fluid Mech.* **153**, 31–58.

Kida, S. & Ohkitani, K. 1992 Spatiotemporal intermittency and instability of a forced turbulence. *Phys. Fluids* A **4**, 1018–1027.

Kim, J. & Antonia, R. A. 1993 Isotropy of the small scales of turbulence at low Reynolds number. *J. Fluid Mech.* **251**, 219–238.

Kistler, A. L. 1952 The vorticity meter. MS Thesis, Johns Hopkins University.

Kit, E., Tsinober, A., Teitel, M., Balint, J. L., Wallace, J. M. & Levich, E. 1988 Vorticity measurements in turbulent grid flows. *Fluid Dyn. Res.* **3**, 289–294.

Kline, S. J. & McClintock, F. A. 1953 Describing uncertainty in single-sample experiments. *Mech. Engng*, January.

Kolmogorov, A. N. 1941 The local structure of turbulence in an incompressible fluid with very large Reynolds numbers. *Dokl. Akad. Nauk. SSSR* **30**, 301 (referred to herein as K41).

Kolmogorov, A. N. 1962 A refinement of previous hypothesis concerning the local structure of turbulence in viscous incompressible fluid at high Reynolds numbers. *J. Fluid Mech.* **13**, 82–85 (referred to herein as K62).

Lemonis, G. C. 1995 An experimental study of the vector fields of velocity and vorticity in turbulent flows. PhD Thesis, Swiss Federal Institute of Technology, Zurich.

Lesieur, M. 1997 *Turbulence in Fluids*, Third Edn. Kluwer.

Moffat, R. J. 1985 Using uncertainty analysis in the planning of an experiment. *Trans. ASME* I: *J. Fluids Engng* **107**, 173–178.

Moffat, R. J. 1988 Describing the uncertainties in experimental results. *Exptl Thermal Fluid Sci.* **1**, 3–17.

Mohamed, M. S. & LaRue, J. C. 1990 The decay power law in grid-generated turbulence. *J. Fluid Mech.* **219**, 195–214.

Monin, A. S. & Yaglom, A. M. 1975 *Statistical Fluid Mechanics*, Vol. 2. MIT Press.

Mydlarski, L. & Warhaft, Z. 1996 On the onset of high-Reynolds-number grid-generated turbulence. *J. Fluid Mech.* **320**, 331–368 (referred to herein as MW).

Noullez, A., Wallace, G., Lempert, W., Miles, R. B. & Frisch, U. 1997 Transverse velocity increments in turbulent flow using the RELIEF technique. *J. Fluid Mech.* **339**, 287–307.

Park, S. R. & Wallace, J. M. 1993 The influence of instantaneous velocity gradients on turbulence properties measured with multi-sensor hot-wire probes. *Exps. Fluids* **16**, 17–26.

Pearson, B. R. & Antonia, R. A. 1997 Velocity structure functions in a turbulent plane jet. *Proc. Eleventh Turbulent Shear Flow Conference, Grenoble*, pp. 3-117–3-121.

Ruetsch, G. R. & Maxey, M. R. 1991 Small-scale features of vorticity and passive scalar fields in homogeneous isotropic turbulence. *Phys. Fluids* A **3**, 1587–1597.

She, Z. S., Jackson, E. & Orszag, S. A. 1990 Intermittent vortex structures in homogeneous isotropic turbulence. *Nature* **344**, 226–228.

She, Z. S. & Leveque, E. 1994 Universal scaling laws in fully developed turbulence. *Phys. Rev. Lett.* **72**, 336–339 (referred to herein as SL).

Sreenivasan, K. R. 1984 On the scaling of the turbulent energy dissipation rate. *Phys. Fluids* **27**, 1048–1051.

Sreenivasan, K. R. 1996 The passive scalar spectrum and the Obukhov-Corrsin constant. *Phys. Fluids* **8**, 189–196.

Sreenivasan, K. R. & Antonia, R. A. 1997 The phenomenology of small-scale turbulence. *Ann. Rev. Fluid Mech.* **29**, 435–472.

Stolovitzky, G. & Sreenivasan, K. R. 1993 Scaling of structure functions. *Phys. Rev.* E **48**, R33–R36.

Taylor, G. I. 1938 Production and dissipation of vorticity in a turbulent fluid. *Proc. R. Soc. Lond.* A **164**, 15–23.

Tennekes, H. & Lumley, J. L. 1972 *A First Course in Turbulence*. MIT Press.

Tsinober, A., Kit, E. & Dracos, T. 1992 Experimental investigation of the field of velocity gradients in turbulent flows. *J. Fluid Mech.* **242**, 169–192 (referred to herein as TKD).

Tutu, N. K. & Chevray, R. 1975 Cross-wire anemometry in high intensity turbulence. *J. Fluid Mech.* **71**, 785–800.

Van Atta, C. W. 1991 Local isotropy of the smallest scales of turbulent scalar and velocity fields. *Proc. R. Soc. Lond.* A **434**, 139–147.

Van Atta, C. W. & Chen, W. 1969 Measurements of spectral energy transfer in grid turbulence. *J. Fluid Mech.* **38**, 743–763.

Vincent, A. & Meneguzzi, M. 1991 The spatial structure and statistical properties of homogeneous turbulence. *J. Fluid Mech.* **225**, 1–20.

Vukoslavcevic, P. & Wallace, J. M. 1981 Influence of velocity gradients on measurements of velocity and streamwise vorticity with hot-wire X-array probes. *Rev. Sci. Instrum.* **52**, 869–879.

Wallace, J. M. 1986 Methods of measuring vorticity in turbulent flows. *Exps. Fluids* **4**, 61–71.

Wallace, J. M. & Foss, J. F. 1995 The measurements of vorticity in turbulent flows. *Ann. Rev. Fluid Mech.* **27**, 467–514.

Wyngaard, J. C. 1971 The effect of velocity sensitivity on temperature derivative statistics in isotropic turbulence. *J. Fluid Mech.* **48**, 763–769.

Yamamoto, K. & Hosokawa, I. 1988 A decaying isotropic turbulence pursued by the spectral method. *J. Phys. Soc. Japan* **57**, 1532–1535.

Zhu, Y. & Antonia, R. A. 1995 Effect of wire separation on X-probe measurements in a turbulent flow. *J. Fluid Mech.* **287**, 199–223.

Zhu, Y. & Antonia, R. A. 1996 Spatial resolution of a 4-X-wire vorticity probe. *Meas. Sci. Technol.* **7**, 1492–1497.

Zhu, Y. & Antonia, R. A. 1997 Correlation between the enstrophy and the energy dissipation rate in a turbulent wake. *Appl. Sci. Res.* **57**, 337–347.